

Probing mixed-state dark matter and $b \rightarrow s\mu^+\mu^-$ anomalies in a scalar-assisted baryonic gauge theory

Taramati^a , Manas Kumar Mohapatra^b , Utkarsh Patel^c , Rukmani Mohanta^b , Sudhanwa Patra^{a,d}

^a*Department of Physics, Indian Institute of Technology Bhilai, Durg-491002, Chhattisgarh, India*

^b*School of Physics, University of Hyderabad, Hyderabad-500046, India*

^c*Saha Institute of Nuclear Physics 1/AF, Salt Lake, Kolkata, 700064, West Bengal, India*

^d*Institute of Physics, Bhubaneswar, Sachivalaya Marg, Bhubaneswar-751005, India*

E-mail: taramati@iitbhilai.ac.in, manasmohapatra12@gmail.com,
utkarsh.patel@saha.ac.in, rmsp@uohyd.ac.in, sudhanwa@iitbhilai.ac.in

ABSTRACT: We explore a Standard Model extension based on a local $U(1)_B$ symmetry, where a baryon-charged scalar mediates interactions between a fermionic dark matter candidate and Standard Model quarks. In this setup, the dark matter relic abundance is shaped not only by standard annihilation channels but also by additional coannihilation processes induced by a new scalar. The presence of this mediator provides a unified link between dark sector and flavor physics, yielding distinctive phenomenological consequences. We conduct a detailed study of dark matter phenomenology, emphasizing the role of the mass splitting between the dark matter particles, and the scalar mediator in determining the efficiency of coannihilation. The parameter space is examined in light of existing constraints from cosmological observations, direct and indirect detection experiments, as well as the collider searches at the LHC. Our analysis shows that the extended scalar sector opens up viable regions of parameter space beyond those accessible in minimal $U(1)_B$ realizations, many of which are expected to be tested by forthcoming searches at XENONnT and CTA. Moreover, the model induces correlated signatures from flavor observables associated with the $b \rightarrow s\mu^+\mu^-$ transitions as well, serving as complementary tests of the underlying framework.

Contents

1	Introduction	2
2	Model Framework	4
2.1	Scalar & gauge sector	6
3	DM Phenomenology	7
3.1	Relic Density and Direct Detection Analysis	9
3.1.1	Relic Density	9
3.1.2	Direct Detection Constraints	14
3.2	In-Direct Signatures	16
4	Flavor Physics Analysis	18
4.1	Effective Hamiltonian	18
4.2	$b \rightarrow s\ell^+\ell^-$ decay observables	19
4.3	Constraint on new physics parameters from $b \rightarrow s\mu^+\mu^-$ transitions	21
5	Summarized discussion: Combined Flavor and DM Analysis	26
6	Conclusion	29
A	Relevant Feynman Diagrams due to extra scalar S_1	30
A.1	Feynman Diagrams Contributing to Relic Density	31
A.2	Relevant Feynman Diagrams with diffused gamma ray production	32
B	Details of the form factors and the angular coefficients for $B \rightarrow (P,V)\ell^+\ell^-$ processes	33
B.1	Form factors for $B \rightarrow (K^{(*)}, \phi)\ell^+\ell^- (\ell = e, \mu, \tau)$	33
B.2	Angular coefficients	34

1 Introduction

The Standard Model (SM) of particle physics, while extremely successful in explaining a wide range of phenomena, fails to account for several key observations, such as the nature of dark matter (DM) [1–8], the observed baryon asymmetry of the Universe, and the possible hints of anomalies in B meson decays. These open questions strongly motivate extensions of the SM based on additional gauge symmetries. In particular, a class of well-motivated models extends the Standard Model gauge group by gauging baryon number (B), lepton number (L), or their certain combinations, giving rise to additional local symmetries such as $U(1)_B$, $U(1)_L$, and others. After a systematic and careful charge assignment to exotic particles, these SM extended gauge groups provide natural, anomaly-free frameworks [3–6]. The lightest mass eigenstate among the exotic fermions, stabilized by a remnant discrete symmetry after $U(1)$ breaking, emerges as a viable DM candidate [9–23].

A particularly compelling set of models involves gauging only the baryon number, leading to an additional $U(1)_B$ gauge symmetry [24]. Such models have been extensively studied in the literature for a wide range of phenomenological motivations [25–30]. In Ref. [25], authors consider a gauged $U(1)_B$ framework with vectorlike fermions and a diquark scalar, in which a residual global symmetry stabilizes a singlet scalar DM candidate with viable relic density and observable direct-detection signatures. In Ref. [26], the authors demonstrate that the exotic decay $Z \rightarrow Z'\gamma$ provides a clean probe of anomalous $U(1)$ gauge symmetries. They show that anomaly-canceling fermions can induce observable, non-decoupling effects that may be accessible at future **TeraZ** experiments. As a result, electroweak precision observables and low-mass dijet searches emerge as complementary probes of baryon number gauge symmetry. Ref. [27] considers a fermionic DM in an asymptotically safe $U(1)_B$ model, where ultraviolet fixed points constrain the gauge coupling and kinetic mixing, yielding a predictive framework compatible with relic density and direct-detection bounds. In Ref. [28], the authors investigate a Dirac DM candidate in a gauged $U(1)_B$ framework, showing that relic density and unitarity constraints impose an upper bound of order 200 TeV on the baryon-number breaking scale. This tight connection between DM and the gauge sector renders the model highly predictive and testable, with implications for baryogenesis. More recently, Refs. [29, 30] studied minimal gauged $U(1)_B$ frameworks in which gauge anomaly cancellation predicts new fermions, including a fermionic DM candidate and a leptophobic gauge boson Z_B . These works emphasized the rich collider phenomenology of such models, highlighting signatures from long-lived charged fermions, multi-lepton final states, while demonstrating consistency with relic density, direct-detection, and LHC constraints. While these studies establish this framework as rich & well-motivated for DM and collider phenomenology, a common study for DM and flavor observables has remained largely unexplored in this context.

With this motivation, the current work extends the minimal $U(1)_B$ framework by introducing an additional singlet scalar field, S_1 , which simultaneously mediates DM interactions and couples to the quark sector. This enables a unified analysis of DM and flavor observables within a consistent gauged $U(1)_B$ theory. Such a combined analysis of DM and flavor physics is particularly timely, as flavor observables can probe energy

scales complementary to those accessed by the next runs of collider experiments, thereby enhancing the discovery potential of gauged $U(1)_B$ models. Nevertheless, our framework can be stringently tested and potentially ruled out by null results from upcoming DM direct detection experiments [31, 32] and/or by precision flavor measurements at upcoming Belle II [33] and LHCb [34] runs. In this study, the presence of S_1 in the scalar sector

Lepton Universality Ratios in $b \rightarrow s\ell^+\ell^-$ Observables				
Decay Observable	q^2 Interval (GeV 2)	SM Prediction	Measured Value	Significance with SM
R_K	[0.1, 1.1]	1 ± 0.01 [35, 36]	$0.994^{+0.090+0.027}_{-0.082-0.029}$ [37]	-
	[1.1, 6.0]	1 ± 0.01 [35, 36]	$0.949^{+0.042+0.023}_{-0.041-0.023}$ [37]	-
$R_{K_S^0}$	[1.1, 6.0]	1 ± 0.01 [35, 36]	$0.66^{+0.20}_{-0.14}$ (stat) $^{+0.02}_{-0.04}$ (syst) [38]	1.4σ
R_{K^*}	[0.045, 1.1]	1 ± 0.01 [35, 36]	$0.927^{+0.093+0.034}_{-0.087-0.033}$ [37]	-
	[1.1, 6.0]	1 ± 0.01 [35, 36]	$1.027^{+0.072+0.027}_{-0.068-0.027}$ (stat) ± 0.047 (syst) [37]	-
$R_{K^{*+}}$	[0.045, 6.0]	1 ± 0.01 [35, 36]	$0.70^{+0.18}_{-0.13}$ (stat) $^{+0.03}_{-0.04}$ (syst) [38]	1.5σ
R_ϕ^{-1}	[0.1, 1.1]	1.016 [39]	$1.57^{+0.28}_{-0.25} \pm 0.05$ [40]	-
	[1.1, 6.0]	1.003 [39]	$0.91^{+0.20}_{-0.19} \pm 0.05$ [40]	-
	[15, 19]	1.002 [39]	$0.85^{+0.24}_{-0.23} \pm 0.10$ [40]	-
Exclusive $b \rightarrow s\mu^+\mu^-$ Observables				
P'_5	[4.0, 6.0]	-0.759 ± 0.071 [41]	$-0.439 \pm 0.111 \pm 0.036$ [42]	3.3σ
	[4.3, 6.0]	-0.795 ± 0.065 [43]	$-0.96^{+0.22}_{-0.21}$ (stat) ± 0.25 (syst) [44]	1.0σ
	[4.0, 8.0]	-0.795 ± 0.054 [45]	$-0.267^{+0.275}_{-0.269}$ (stat) ± 0.049 (syst) [46]	2.1σ
$\mathcal{B}(B^+ \rightarrow K^+\mu^+\mu^-)$	[1.1, 6.0]	$(1.708 \pm 0.283) \times 10^{-7}$ [47]	$(1.186 \pm 0.034 \pm 0.059) \times 10^{-7}$ [37]	4.2σ
$\mathcal{B}(B^0 \rightarrow K^{0*}\mu^+\mu^-)$	[1.1, 6.0]	$(2.323 \pm 0.381) \times 10^{-7}$ [48]	$(2.018 \pm 0.100 \pm 0.053) \times 10^{-7}$ [49]	-
$\mathcal{B}(B_s \rightarrow \phi\mu^+\mu^-)$	[1.1, 6.0]	$(2.647 \pm 0.319) \times 10^{-7}$ [48, 50]	$(1.41 \pm 0.073 \pm 0.024 \pm 0.068) \times 10^{-7}$ [51–53]	3.6σ
$\mathcal{B}(B_s \rightarrow \mu^+\mu^-)$	-	$(3.672 \pm 0.154) \times 10^{-9}$ [54, 55]	$(3.361 \pm 0.028) \times 10^{-9}$ [56]	-

Table 1: Status of $b \rightarrow s\ell^+\ell^-$ decay observables with SM predictions and experimental results.

has a significant impact on the phenomenology of DM. Depending on the charge assignment and coupling strengths, the new scalar can itself be a viable mediator in interactions between the dark sector and the SM particles. This influences the DM relic abundance through modified annihilation or co-annihilation channels, and alters predictions for direct and indirect detection experiments.

In addition to its implications for DM phenomenology, the framework considered in this work naturally gives rise to nontrivial effects in flavor physics. In particular, new particles and interactions that couple the dark sector to SM fermions can generate flavor-changing neutral-current (FCNC) processes at the loop level. Such transitions are suppressed in the SM and therefore provide a sensitive indirect probe of physics beyond it. Among the FCNC processes, the quark-level transition $b \rightarrow s\ell^+\ell^-$ plays a central role due to its contribution to a wide range of experimentally accessible observables, including branching ratios, angular distributions, and lepton flavor universality (LFU) tests. In recent years, measurements of these observables by the LHCb and Belle collaborations have revealed a pattern of deviations from the SM predictions in several channels. While the latest measurements of the LFU ratios R_K and R_{K^*} are consistent with the SM expectations, the discrepancies still persist in the celebrated angular observable P'_5 , and in the differential branching fractions of several

decay modes such as, $B_s \rightarrow \phi \mu^+ \mu^-$ and $B^+ \rightarrow K^+ \mu^+ \mu^-$. A concise summary of the current experimental status of the relevant $b \rightarrow s \ell^+ \ell^-$ observables, together with their Standard Model predictions, is presented in Table 1. These anomalies can be explained by new interactions that contribute to semileptonic $b \rightarrow s \ell^+ \ell^-$ ($\ell = e, \mu$) transitions, which may also play a role in governing DM interactions. This observation motivates a combined analysis of DM and flavor observables within a specific and unified theoretical framework. In contrast to the explicitly leptophilic scenarios explored in Refs. [57–61], which rely on leptoquarks, Z' bosons, or inert scalar doublets with direct couplings to charged leptons, our framework is based on a predominantly leptophobic mixed-state DM setup. The new mediator couples primarily to quarks and the dark sector, while interactions with charged leptons arise only indirectly, for example, through mixing effects. As a result, the $b \rightarrow s \mu^+ \mu^-$ transitions are generated in a controlled and predictive manner, allowing flavor observables to probe the same underlying dynamics responsible for DM interactions. Although the authors in Ref. [62] have addressed the $b \rightarrow s \mu^+ \mu^-$ anomalies, focusing on mixed-state frameworks with vector-like particles and leptoquarks, this mainly affects their contributions to the semileptonic operators. In contrast, our analysis is performed within a concrete, well-defined model in which the mediator structure is explicitly connected to the dark sector. This enables a detailed study of exclusive decay modes and angular observables in $b \rightarrow s \mu^+ \mu^-$ transitions, while simultaneously correlating flavor constraints with DM phenomenology. Consequently, our framework provides complementary signatures beyond those accessible in purely leptophilic constructions.

The outline of the paper is as follows. In Section 2, we introduce the theoretical framework of the model and discuss its particle content, relevant Lagrangian, and the scalar and gauge sectors. DM phenomenology, including relic density computation, direct detection constraints, and indirect signatures, is presented in Section 3. In Section 4, we perform a comprehensive flavor physics analysis focusing on $b \rightarrow s \mu^+ \mu^-$ transitions. The combined numerical results exploring correlations between flavor physics analyses and DM observables, and their phenomenological implications, are discussed in Section 5. Finally, we present the conclusion of the work in Section 6 while an appendix is also provided at the end.

2 Model Framework

The baryonic gauge extension of the SM, in which the baryon number is promoted to a local $U(1)_B$ symmetry, has been thoroughly explored in our earlier works [5, 6]. To ensure the cancellation of gauge anomalies, the model introduces exotic fermions: a pair of $SU(2)_L$ doublets

$$\Psi_L [1_c, 2_L, \frac{1}{2}Y, -1_B] \sim \begin{pmatrix} \Psi_L^+ \\ \Psi_L^0 \end{pmatrix}, \quad \Psi_R [1_c, 2_L, \frac{1}{2}Y, 2_B] \sim \begin{pmatrix} \Psi_R^+ \\ \Psi_R^0 \end{pmatrix}, \quad (2.1)$$

two pairs of singlets

$$\xi_L [1_c, 1_L, 1_Y, 2_B], \quad \xi_R [1_c, 1_L, 1_Y, -1_B], \quad (2.2)$$

and

$$\chi_L^0 [1_c, 1_L, 0_Y, 2_B], \quad \chi_R^0 [1_c, 1_L, 0_Y, -1_B], \quad (2.3)$$

where the numbers in the bracket represent the charges under $SU(3)_c \times SU(2)_L \times U(1)_Y \times U(1)_B$ gauge group. The baryonic charges are assigned such that $B_1 - B_2 = -3$. In addition, one extra scalar field

$$S [1_c, 1_L, 0_Y, -3_B] \quad (2.4)$$

is required to break the extended gauge symmetry spontaneously. After $U(1)_B$ breaking, the neutral components of $\chi_{L/R}^0$ and $\Psi_{L/R}^0$ mix to form two Dirac fermions (Ψ_1, Ψ_2) , where the lighter state Ψ_1 naturally emerges as a viable DM candidate. A comprehensive discussion of anomaly cancellation, fermion charge assignments, and the diagonalization of the resulting mass matrices is provided in [5, 6].

In continuation of our previous work on the singlet-doublet fermionic DM (SDFDM) framework [5], we consider an extension of the model by introducing an additional scalar field, denoted as S_1 . This scalar transforms as $(\mathbf{3}_c, \mathbf{1}_L, -\mathbf{1}/\mathbf{3}_Y, -\mathbf{5}/\mathbf{3}_B)$ under the $SU(3)_c \times SU(2)_L \times U(1)_Y \times U(1)_B$ gauge group. While being a singlet under the electroweak $SU(2)_L$ symmetry, it carries non-trivial charges under $SU(3)_C$ and $U(1)_B$, making it a colored scalar state.

The motivation for introducing S_1 is twofold:

- To explore the possible interplay between DM and flavor physics observables, by allowing new interactions that can mediate the rare FCNC decays.
- To explore the phenomenological implications of the additional scalar S_1 in the context of DM, particularly its influence on the relic abundance, direct detection cross-sections, and potential indirect detection signatures.

The field content of exotic fermions and their gauge charge assignments remain identical to those defined in Ref. [5], ensuring the anomaly cancellation conditions are satisfied. The extended model introduces the following Yukawa interaction term involving the new scalar S_1 :

$$\mathcal{L}_{\text{Yukawa}} \supset Y_{S_1} \bar{q} S_1 \Psi_R + \text{h.c.}, \quad (2.5)$$

where q represents the SM quark left-handed doublet, Ψ_R is the exotic right-handed fermion from the SDFDM sector, and Y_{S_1} denotes the corresponding Yukawa coupling. This Lagrangian term not only induces new interactions relevant to flavor-physics processes but also facilitates interactions between the visible and dark sectors, thereby influencing DM phenomenology. Additionally, the scalar S_1 contributes to new processes that affect DM production and detection mechanisms, thereby enriching the phenomenology of the SDFDM framework. Including the S_1 interaction given above in Eq. (2.5), the relevant kinetic terms and Yukawa Lagrangian involving all the exotic fermions of the framework is given by:

$$\begin{aligned} \mathcal{L} = & \overline{\Psi_L} i \not{D} \Psi_L + \overline{\Psi_R} i \not{D} \Psi_R + \overline{\chi_L} i \not{D} \chi_L + \overline{\chi_R} i \not{D} \chi_R + \overline{\xi_L} i \not{D} \xi_L + \overline{\xi_R} i \not{D} \xi_R \\ & - h_1 \overline{\Psi_L} \tilde{H} \xi_R - h_2 \overline{\Psi_R} \tilde{H} \xi_L - h_3 \overline{\Psi_L} H \chi_R - h_4 \overline{\Psi_R} H \chi_L \\ & - \lambda_\Psi \overline{\Psi_L} S \Psi_R - \lambda_\xi \overline{\xi_L} \tilde{S} \xi_R - \lambda_\chi \overline{\chi_L} \tilde{S} \chi_R + Y_{S_1} \bar{q} S_1 \Psi_R. \end{aligned} \quad (2.6)$$

2.1 Scalar & gauge sector

Within the current framework, we extend the scalar sector by introducing an additional scalar field, S_1 . This scalar S_1 can interact with scalar S and the SM Higgs doublet H at tree level. Accordingly, the most general renormalizable scalar potential consistent with the symmetries of the model can be written as:

$$V(H, S, S_1) = -\mu_H^2 H^\dagger H + \lambda_H (H^\dagger H)^2 - \mu_S^2 S^\dagger S + \lambda_S (S^\dagger S)^2 - \mu_{S_1}^2 S_1^\dagger S_1 + \lambda_{S_1} (S_1^\dagger S_1)^2 + \lambda_{HS} (S^\dagger S)(H^\dagger H) + \lambda_{HS_1} (S_1^\dagger S_1)(H^\dagger H) + \lambda_{SS_1} (S_1^\dagger S_1)(S^\dagger S), \quad (2.7)$$

where λ_{HS} , λ_{SS_1} and λ_{HS_1} are portal coupling strengths. Upon the spontaneous breaking of the associated symmetries, the scalar fields H and S acquire nonzero vacuum expectation values v and v_B , respectively. In contrast, the scalar S_1 is inert and does not acquire a VEV. The mass matrix for these scalars in the eigenbasis (H, S, S_1) can be written as:

$$M_{HSS_1}^2 = \begin{pmatrix} 2\lambda_H v^2 & \lambda_{HS} v v_B & 0 \\ \lambda_{HS} v v_B & 2\lambda_S v_B^2 & 0 \\ 0 & 0 & -\mu_{S_1}^2 + \frac{1}{2}\lambda_{HS_1} v^2 + \frac{1}{2}\lambda_{SS_1} v_B^2 \end{pmatrix}, \quad (2.8)$$

After matrix diagonalization, the mass eigenvalues in the basis (h, s, S_1) are given as:

$$\begin{aligned} m_h^2 &= v^2 \lambda_H + v_B^2 \lambda - \sqrt{(v^2 \lambda_H - v_B^2 \lambda)^2 + (\lambda_{HS} v v_B)^2}, \\ m_s^2 &= v^2 \lambda_H + v_B^2 \lambda + \sqrt{(v^2 \lambda_H - v_B^2 \lambda)^2 + (\lambda_{HS} v v_B)^2}, \\ m_{s_1}^2 &= -\mu_{S_1}^2 + \frac{1}{2}\lambda_{HS_1} v^2 + \frac{1}{2}\lambda_{SS_1} v_B^2. \end{aligned} \quad (2.9)$$

Here, $m_h \simeq 125$ GeV is the mass of the SM-like Higgs particle. The mixing between physical states h and s can be parameterized by a θ mixing angle defined by

$$\tan(2\theta) = \frac{\lambda_{HS} v v_B}{\lambda_H v^2 - \lambda_S v_B^2}, \quad (2.10)$$

which arises from diagonalizing the (H, S) sub-matrix from Eq. (2.8). The scalar masses can be recast in terms of the θ angle as,

$$\begin{aligned} m_h^2 &= 2v^2 \lambda_H \cos^2 \theta + 2v_B^2 \lambda \sin^2 \theta + \lambda_{HS} v v_B \sin 2\theta, \\ m_s^2 &= 2v^2 \lambda_H \sin^2 \theta + 2v_B^2 \lambda \cos^2 \theta - \lambda_{HS} v v_B \sin 2\theta. \end{aligned} \quad (2.11)$$

From Eq. (2.8), it can be seen that S_1 does not mix with the other scalars; thus, the mass eigenstate s_1 is purely derived from the S_1 field. Hence, for the remainder of this paper, we may interchangeably use S_1 and s_1 , as both refer to the same physical state. In the subsequent sections, we present a detailed analysis of the implications of the new scalar S_1 on flavor physics observables, including its potential contributions to flavor-changing processes and rare decays. Furthermore, we investigate its impact on DM phenomenology,

focusing on the relic abundance, direct detection prospects, and possible indirect detection signatures arising from its interactions.

In the gauge sector, the presence of the additional scalar S_1 does not modify the mass spectrum of the electroweak gauge bosons Z and W^\pm , nor the mass of the extra gauge boson Z' associated with the $U(1)_B$ symmetry (see Ref. [5, 6] for more details). In our analysis, we neglect the kinetic mixing between the $U(1)_Y$ and $U(1)_B$ gauge groups. This approximation is justified by current experimental bounds, which tightly constrain the kinetic mixing parameter and render its effects on the gauge boson masses and couplings phenomenologically sub-leading within the parameter space considered [63–65]. Under the zero kinetic mixing assumption, the mass of Z' is given by,

$$M_{Z'} = 3g_B v_B \quad (2.12)$$

3 DM Phenomenology

With the extended model setup introduced in the previous section, we further explore the framework’s phenomenological relevance. In particular, we focus on two crucial aspects: the impact of the new scalar field S_1 on DM observables, and its role in flavor physics, including possible contributions to the rare FCNC decays. The S_1 Yukawa interaction connects the dark matter and flavor sectors via the loop-level flavor observables.

Throughout our analysis, we also emphasize the impact of scalar S_1 and of various mass splittings in the dark sector on the DM-related phenomenology. The Feynman diagrams relevant to DM annihilation involving scalar S_1 are provided in Figure 12, and the relevant co-annihilations involving S_1 and other dark sector particles are provided in Figure 13 in the Appendix. The fermionic mass eigenstate Ψ_1 is taken to be the stable dark matter candidate, with properties determined by singlet–doublet mixing (see Ref. [5]). The presence of the extra scalar S_1 potentially has a significant impact, since it alters DM annihilation channels and modifies DM scattering rates with nucleons. Thus, the relevant input parameters are:

$$M_{\Psi_1}, \quad M_{Z'}, \quad \Delta M(\Psi_2, \Psi_1), \quad \sin \theta_{\text{DM}}, \quad v_B, \quad m_{S_1}, \quad \Delta M(S_1, \Psi_1), \quad Y_{S_1}, \quad (3.1)$$

where M_{Ψ_1} is the DM mass, $M_{Z'}$ is the mass of the leptophobic gauge mediator, $\Delta M(\Psi_2, \Psi_1)$ is the splitting between exotic neutral fermions, θ_{DM} is the DM mixing angle, v_B is the $U(1)_B$ breaking scale, m_{S_1} is the scalar mass, $\Delta M(S_1, \Psi_1)$ is the mass gap between S_1 and DM, and Y_{S_1} is the Yukawa coupling strength for the Lagrangian term in Eq. (2.5).

To study DM phenomenology, we implement the model in **SARAH** [66] package, generate the spectrum with **SPheno** [67], and perform numerical computations of relic abundance and cross-sections using **micrOMEGAs** [68] code. This methodology enables us to systematically track the impact of the new scalar sector on both DM and flavor phenomenology. In the following discussion, we perform three key analyses: the relic density calculation, constraints from direct searches, and possible indirect detection signals, with an emphasis on the roles of S_1 and dark-sector mass splittings in shaping the allowed parameter space.

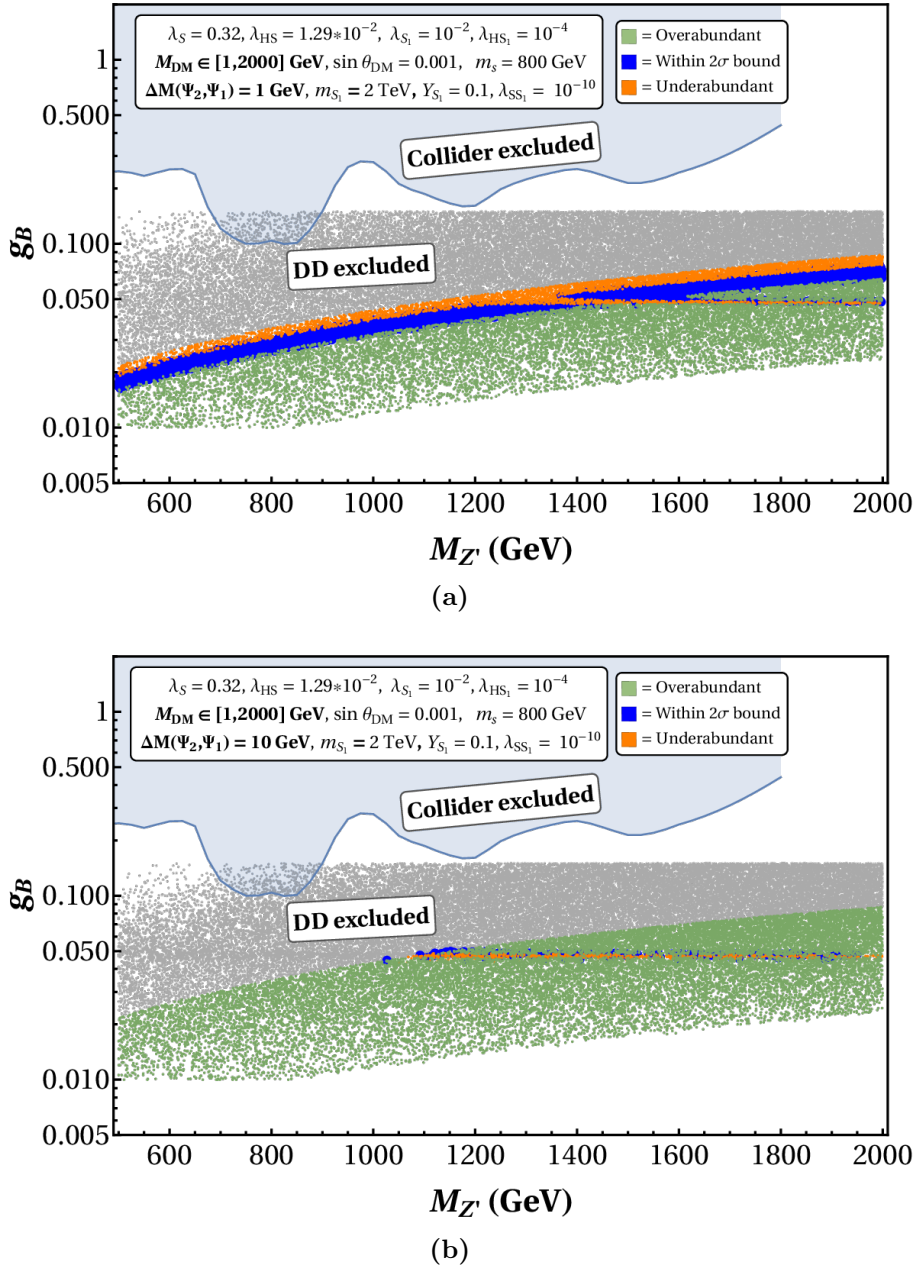


Figure 1: Parameter space in the $(M_{Z'}, g_B)$ plane for two benchmark scenarios. The relic density constraint from Planck is indicated by the color coding: green points correspond to overabundant DM, orange points lie within the 2σ allowed range, and blue points give underabundant relic density. The gray shaded area is excluded by direct-detection (DD) bounds from LZ (2022, while the light-blue shaded region is ruled out by collider searches for a heavy Z' boson. **Top panel (a):** mass splitting $\Delta M(\Psi_2, \Psi_1) = 1$ GeV. **Bottom panel (b):** mass splitting $\Delta M(\Psi_2, \Psi_1) = 10$ GeV. Other relevant parameters are fixed as $\lambda_S = 0.32$, $\lambda_{HS} = 1.29 \times 10^{-2}$, $\lambda_{S_1} = 10^{-2}$, $\lambda_{HS_1} = 10^{-4}$, $\lambda_{SS_1} = 10^{-10}$, $\sin \theta_{DM} = 0.001$, $m_s = 800$ GeV, $m_{S_1} = 2$ TeV, and $Y_{S_1} = 0.1$. The DM mass is varied within the range of 1 GeV to 2 TeV.

3.1 Relic Density and Direct Detection Analysis

In this sub-section, we study the impact of variations of model input parameters on the DM final relic, the obtained DD cross section, and the associated phenomenology. Specifically, we examine the effects of changing the mass splittings $\Delta M(\Psi_2, \Psi_1)$, $\Delta M(S_1, \Psi_1)$, and coupling Y_{S_1} . The parameter scans and their associated plots presented ahead are generated by fixing certain input parameters: $\lambda_S = 0.32$, $\lambda_{HS} = 1.29 \times 10^{-2}$, $\sin \theta_{\text{DM}} = 0.001$, $m_s = 800$ GeV, $m_{S_1} = 2$ TeV, $\lambda_S = 1 \times 10^{-2}$ and $\lambda_{HS_1} = 1 \times 10^{-4}$. The choice of these input parameter values is motivated partly by earlier studies. To enable a direct comparison, we keep few benchmark values identical to those employed in Refs. [5, 6]. For some other parameters like λ_{HS_1} , m_{S_1} , representative values are chosen within their allowed ranges, since the impact of their variation is not the focus of this study and may be taken up in a future work. The coupling λ_{SS_1} is set at a small value of 1×10^{-10} to ensure a negligible contribution of scalar S 's VEV (v_B) on the mass of the S_1 .

3.1.1 Relic Density

Firstly, we depict two scatter plots in Figure 1, highlighting the allowed parameter space in the $(M_{Z'}, g_B)$ plane from DM relic, direct detection, and Z' collider searches over a range of DM mass. In the top panel (Figure 1a) where $\Delta M(\Psi_2, \Psi_1) = 1$ GeV, for small values of g_B , we see that although this region is allowed by both direct detection and collider searches, a significant portion of the parameter points here result in DM overabundance (green shaded region) and is thus excluded by the DM relic requirements. For intermediate g_B values, a narrow band of blue points (within 2σ DM relic) is also present in the plot for the entire range of Z' mass, which depicts the Z' resonance region for DM candidate, i.e., where $M_{\text{DM}} \simeq M_{Z'}/2$. It corresponds to a significantly enhanced DM annihilation via the s -channel Z' pole, yielding the correct DM relic density with observations. This blue region is particularly interesting since it shows the portion of parameter space where DM survives all existing constraints from relic requirements (Planck 2018 [69]), direct detection (LZ 2022 [70]), and collider searches (ATLAS), and thus constitutes a phenomenologically viable region in the upcoming experiments like XENONnT. At larger g_B values, the annihilation cross section becomes too efficient, and for most of the parameter points here, we obtain an underabundant DM relic (orange and gray shaded regions). The orange points correspond to plot points that remain consistent with the LZ and collider constraints but produce underabundant DM. In the gray region, in addition to being underabundant, the DM is also ruled out by the LZ data.

The obtained plot behavior changes noticeably when $\Delta M(\Psi_2, \Psi_1)$ is increased to 10 GeV (bottom panel, Figure 1b) while keeping other input parameters the same as those in Figure 1a. In this case, with the increased mass splitting, the strength of DM co-annihilations with the next-to-lightest state, Ψ_2 , becomes less significant, leading to a larger number of plot points where the DM relic is overabundant (green shaded region). Consequently, most of the points of interest (in comparison with Figure 1a) drop out from the 2σ relic region here, and only a handful of points appear that are viable with all the phenomenological requirements (blue colored points). Again, for larger values of g_B ,

most of the points are excluded by the LZ 2022, as indicated by the gray-shaded region. Overall, the figure demonstrates that the Z' resonance region provides the most interesting region of parameter space in the $M_{Z'} - g_B$ plane, with a clear dependence on the dark-sector mass splitting. Next, in Figure 2 we show the relic abundance Ωh^2 in the

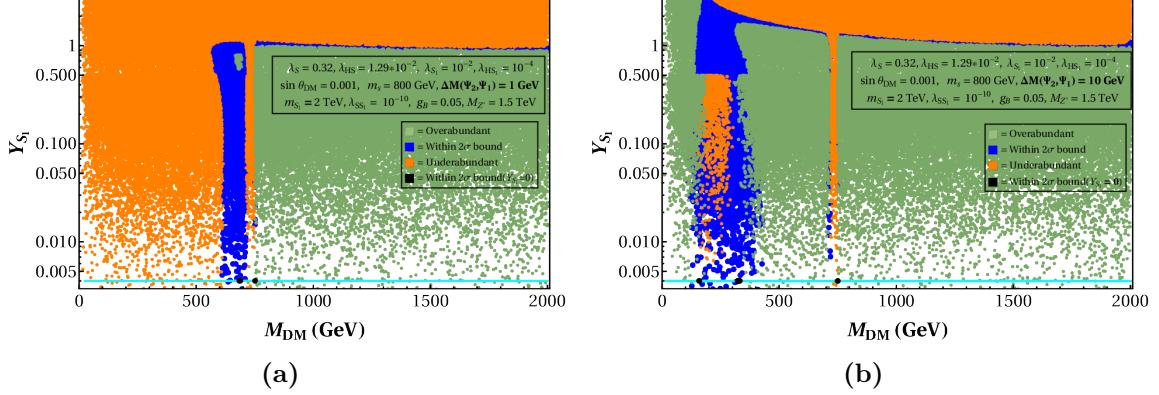


Figure 2: The relic abundance Ωh^2 in the $M_{\text{DM}} - Y_{S_1}$ plane for two different choices of mass splitting $\Delta M(\Psi_2, \Psi_1)$. **Left** (a) $\Delta M(\Psi_2, \Psi_1) = 1 \text{ GeV}$, **Right** (b) $\Delta M(\Psi_2, \Psi_1) = 10 \text{ GeV}$. The color code indicates the relic density: green points are over-abundant, blue points lie within the 2σ bound of the observed value ($\Omega h^2 \simeq 0.110 \pm 0.012$), and orange points are under-abundant. The analysis is performed with fixed parameters: $\lambda_S = 0.32$, $\lambda_{HS} = 1.29 \times 10^{-2}$, $\lambda_{S_1} = 10^{-2}$, $\lambda_{HS_1} = 10^{-4}$, $\lambda_{SS_1} = 10^{-10}$, $\sin \theta_{\text{DM}} = 0.001$, $m_s = 800 \text{ GeV}$, $m_{S_1} = 2 \text{ TeV}$, $M_{Z'} = 1.5 \text{ TeV}$, and $g_B = 0.05$. All displayed points are consistent with direct-detection limits from the LZ 2022 data.

$M_{\text{DM}} - Y_{S_1}$ plane for two benchmark mass splittings, $\Delta M(\Psi_2, \Psi_1) = 1 \text{ GeV}$ (left panel plot 2a) and $\Delta M(\Psi_2, \Psi_1) = 10 \text{ GeV}$ (right panel plot 2b). The fixed input parameters for these plots are: $\lambda_S = 0.32$, $\lambda_{HS} = 1.29 \times 10^{-2}$, $\lambda_{S_1} = 10^{-2}$, $\lambda_{HS_1} = 10^{-4}$, $\lambda_{SS_1} = 10^{-10}$, $\sin \theta_{\text{DM}} = 0.001$, $m_s = 800 \text{ GeV}$, $m_{S_1} = 2 \text{ TeV}$, $g_B = 0.05$ and $M_{Z'} = 1.5 \text{ TeV}$. All points shown satisfy the projected direct-detection sensitivities from the most stringent LZ data. The color coding classifies the obtained relic abundance as: green color reflects DM over-abundance, blue points are within the Planck 2σ band, and orange color corresponds to DM under-abundance. For both plots, the vertical features (sharp, nearly vertical blue bands) reflect the regions of resonant enhancements of the DM annihilation cross section. In our parameter space of interest, there are two evident resonance regions: the Z' pole at $M_{\text{DM}} \simeq M_{Z'}/2$ (visible near $M_{\text{DM}} \simeq 0.75 \text{ TeV}$ for $M_{Z'} = 1.5 \text{ TeV}$ in both plots) and a pole emerging from exotic scalar S mediated interactions at $M_{\text{DM}} \simeq m_s/2$ (visible near $M_{\text{DM}} \simeq 400 \text{ GeV}$ for $m_s = 800 \text{ GeV}$ in the right panel plot). In the left panel (Figure 2a), where the splitting is fixed to $\Delta M(\Psi_2, \Psi_1) = 1 \text{ GeV}$, the coannihilation channels remain highly efficient in the low DM mass region up to about 800 GeV, independent of the value of the Yukawa coupling Y_{S_1} . As a result, the scalar resonance pole is absent, and the strong DM co-annihilations via Ψ_2 drive the final DM relic to be underabundant here. Beyond this scale, the coannihilation channels are suppressed, leading to overabundant regions at higher DM masses (indicated by green points). In this regime, the coannihilation rate is significant, and the relic density requirement is satisfied only for relatively larger values

of the Yukawa coupling, typically $Y_{S_1} \sim 1$ (thin blue horizontal curve around $Y_{S_1} \sim 1$ in Figure 2a).

Increasing the splitting to $\Delta M(\Psi_2, \Psi_1) = 10$ GeV, shown in the right panel (Figure 2b), suppresses the strength of Ψ_2 assisted co-annihilations. Consequently, apart from the Z' and scalar S resonance regions, the parameter space mostly produces an overabundance of final DM relic (green regions) up to a value of 1 for Y_{S_1} . However, when Y_{S_1} exceeds unity, the interaction term $Y_{S_1} \bar{q} S_1 \Psi_R$ becomes significant, reactivating co-annihilation channels and opening up allowed regions consistent with relic density bounds. For even larger values of Y_{S_1} , the annihilation cross section is strongly enhanced, driving the relic abundance into the underabundant regime, as reflected in the extended orange region towards the top side of the plot. A robust feature across both panels is the vertical band near $M_{\text{DM}} \simeq M_{Z'}/2$, originating from the Z' -mediated resonance. The plots also depict the role of the Yukawa coupling Y_{S_1} on the final DM relic abundance. This coupling controls the strength (and width) of S_1 scalar-mediated DM annihilations. It is evident that non-zero values of Y_{S_1} allow a larger region of parameter space to produce a final DM relic within the Planck 2σ limit (blue colored regions). For a direct comparison, we have also plotted the obtained DM relic for the case where Y_{S_1} is set to zero (horizontal cyan lines), and the regions of parameter space where the obtained final relic falls within a 2σ bound are marked by black dots. Thus, the mass splitting $\Delta M(\Psi_2, \Psi_1)$, together with the Yukawa coupling Y_{S_1} , plays a crucial role in shaping the viable parameter space.

The scatter plots in Figures 3 and 4 illustrate the dependence of the relic abundance on the mass splittings $\Delta M(\Psi_2, \Psi_1)$ and $\Delta M(S_1, \Psi_1)$ for two different choices of the Z' mass: $M_{Z'} = 1.5$ TeV (Figure 3) and $M_{Z'} = 1$ TeV (Figure 4). Each subplot corresponds to a different value of DM mass, with $M_{\text{DM}} = 100, 500, 800, 1000$ GeV for subplots 3a, 3b, 3c, and 3d, respectively, and $M_{\text{DM}} = 100, 400, 600, 800$ GeV for subplots 4a, 4b, 4c, and 4d, respectively. The remaining parameters are kept fixed at $\lambda_S = 0.32$, $\lambda_{HS} = 1.29 \times 10^{-2}$, $\lambda_{S_1} = 10^{-2}$, $\lambda_{HS_1} = 10^{-4}$, $\lambda_{SS_1} = 10^{-10}$, $\sin \theta_{\text{DM}} = 0.001$, $m_s = 800$ GeV, $m_{S_1} = 2$ TeV, and $Y_{S_1} = 0.1$ for all the plots. Blue points correspond to Planck 2σ allowed region, while orange (green) points denote underabundant (overabundant) DM. Direct detection and collider constraints are always satisfied in the shown parameter space due to the small gauge coupling $g_B = 0.05, 0.033$ and the suppressed scalar mixing, $\sin \theta = 0.001$. Below, we discuss the characteristic features obtained in these plots for representative benchmark values of M_{DM} as different cases.

Case I: $M_{\text{DM}} = 100$ GeV (Figure 3a and Figure 4a)

In this case, the DM mass lies well below both the scalar S resonance ($m_s/2 = 400$ GeV) and the Z' resonance ($M_{Z'}/2 = 750$ GeV). Thus, DM annihilations alone are inefficient to provide the correct relic abundance at freeze-out. However, when one of the mass splittings is very small, co-annihilation channels assisted via Ψ_2 or S_1 become sufficiently efficient to produce the observed relic abundance, resulting in a narrow 'L' shaped blue strip visible in the plots. For even smaller mass splittings, the DM depletion becomes too efficient, and the final relic falls into the under-abundant region (orange points). When both the

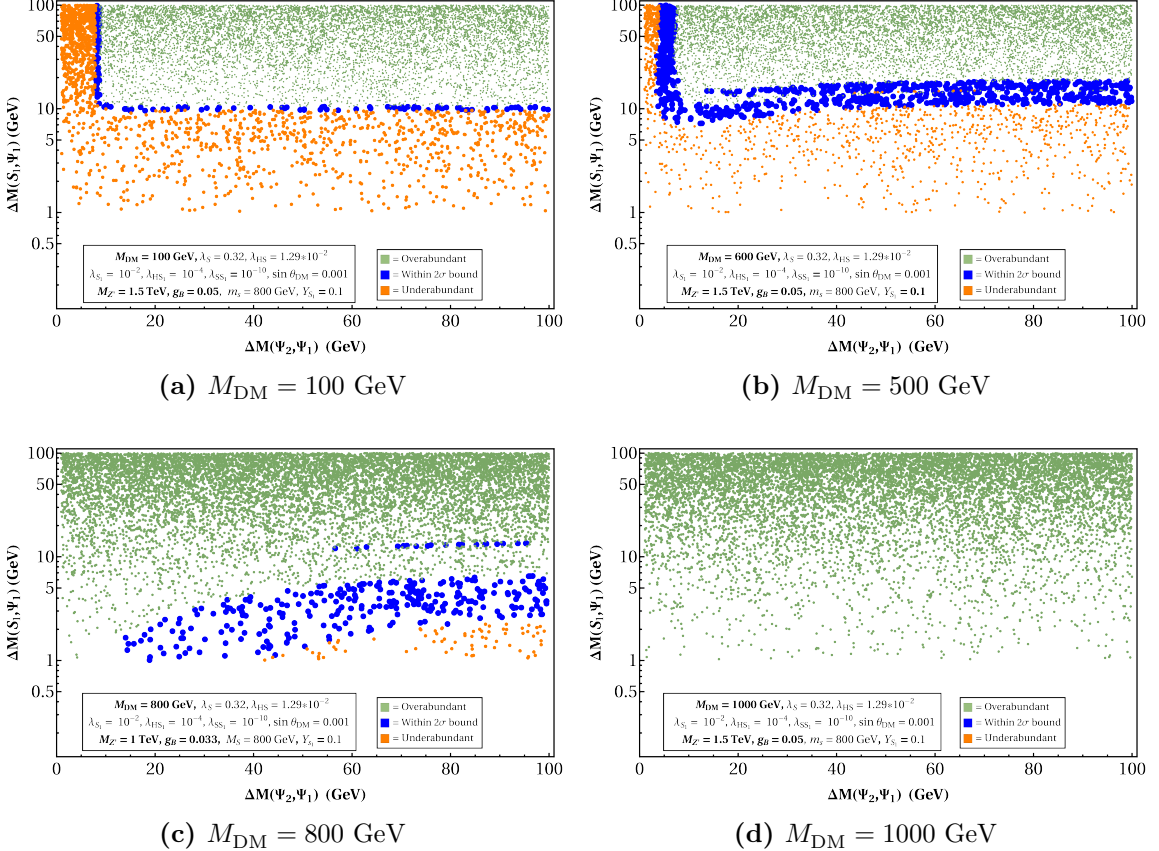


Figure 3: Relic density allowed parameter space in the $\Delta M(\Psi_2, \Psi_1)$ – $\Delta M(S_1, \Psi_1)$ plane for different DM masses: (a) $M_{\text{DM}} = 100$ GeV, (b) $M_{\text{DM}} = 500$ GeV, (c) $M_{\text{DM}} = 800$ GeV, and (d) $M_{\text{DM}} = 1000$ GeV with fixed gauge boson mass $M_{Z'} = 1.5$ TeV. The color coding denotes overabundant (green), underabundant (orange), and points consistent with the observed relic density within 2σ (blue). All displayed points are consistent with direct detection limits from experiments such as LZ 2022.

mass splittings become large enough, then, as expected, most of the parameter space is overabundant (green points). No other interesting plot features appear here.

Case II: $M_{\text{DM}} = 400, 500, 600$ GeV (Figures 3b, 4b and 4c, respectively)

In this case, the DM mass lies close to both the scalar resonance at $m_s/2 = 400$ GeV and the Z' resonance at $M_{Z'}/2 = 750$ GeV. As a result, resonant annihilation channels become active and significantly enhance the annihilation cross section at freeze-out. In addition, for small mass splittings, co-annihilation processes further enhance DM depletion, allowing the correct relic abundance to be achieved over a larger region of parameter space. This results in an extended blue band of relic-density-allowed points spanning a substantial portion of the plot. We further find that, in this regime, the relic density remains mostly insensitive to variations in $M_{Z'}$ (compare Figures 3b and 4c).

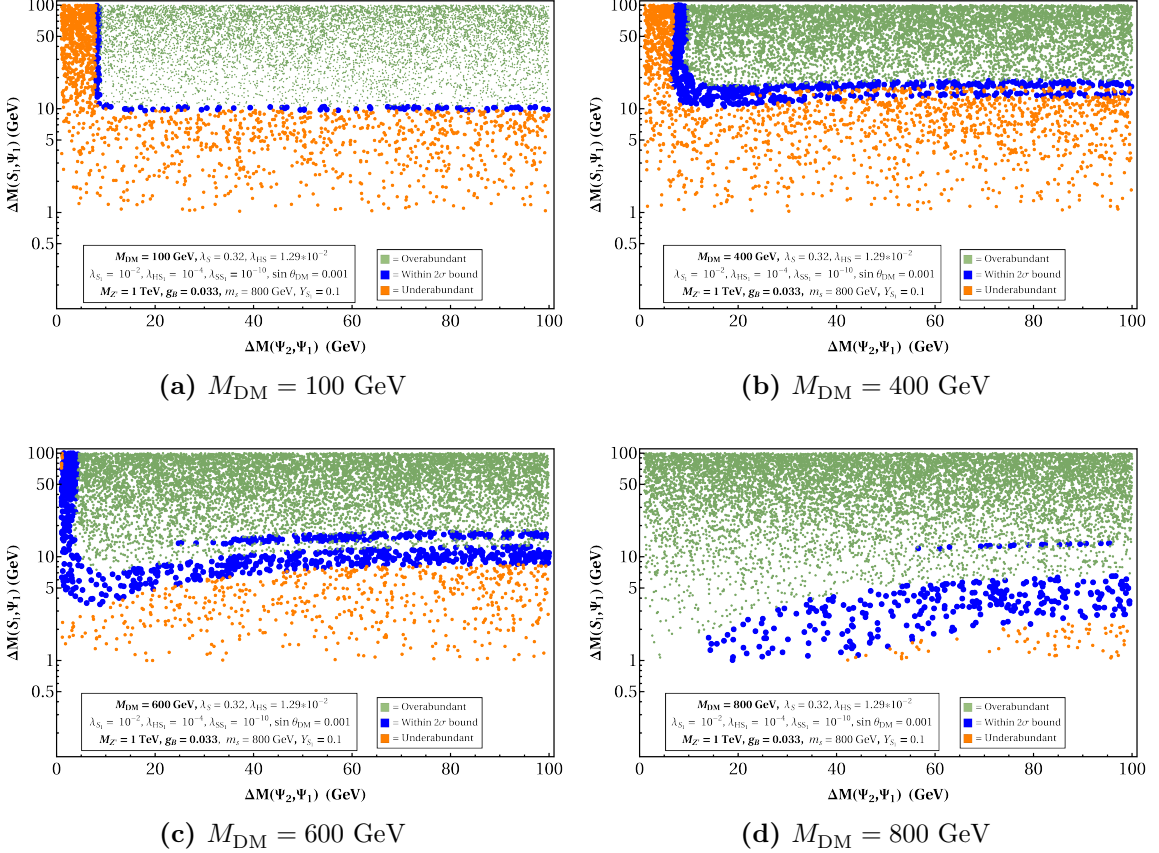


Figure 4: Relic density allowed parameter space in the $\Delta M(\Psi_2, \Psi_1)$ – $\Delta M(S_1, \Psi_1)$ plane for different DM masses: (a) $M_{\text{DM}} = 100$ GeV, (b) $M_{\text{DM}} = 400$ GeV, (c) $M_{\text{DM}} = 600$ GeV, and (d) $M_{\text{DM}} = 800$ GeV with fixed gauge boson mass $M_{Z'} = 1$ TeV. The color coding denotes overabundant (green), underabundant (orange), and points consistent with the observed relic density within 2σ (blue). All displayed points are consistent with direct detection limits from experiments such as LZ 2022.

Case III: $M_{\text{DM}} = 800$ GeV (Figure 3c and Figure 4d)

In this case, the DM mass is nearly degenerate with the scalar partner ($m_s = 800$ GeV) and close to the Z' pole, ($M_{Z'}/2 = 750$ GeV). Thus, the scalar coannihilations majorly set the obtained DM relic. This explains the diagonal distribution of blue points, reflecting the condition $\Delta M(S_1, \Psi_1) \simeq \Delta M(\Psi_2, \Psi_1)$, where multiple states contribute simultaneously to the freeze-out DM abundance. For larger mass splittings, the strength of co-annihilation channels weakens, and the relic density becomes too large (green region). In this scenario, the results again show no significant dependence on Z' mass (compare Figures 3b and 4c).

Case IV: $M_{\text{DM}} = 1000$ GeV (Figure 3a and Figure 3a)

In this regime, the DM mass lies above the scalar mass and far from the Z' resonance. Both annihilation and coannihilation channels are inefficient, and as a result, the relic density is always too large. Hence, no viable parameter points remain (i.e., all are overabundant).

Overall from Figures 3 and 4, we observe that at low M_{DM} (< 400 GeV), co-annihilations via Ψ_2 and S_1 can play a crucial role in deciding the obtained relic abundance, while at intermediate masses ($400 - 800$ GeV), resonance-assisted DM annihilations provide large allowed regions from the DM relic. For high DM masses (> 800 GeV), both annihilation and co-annihilation become inefficient, leading to predominantly overabundant final relics.

3.1.2 Direct Detection Constraints

Direct detection searches are among the most concrete approaches for detecting particle DM candidates. They aim to observe possible nuclear recoils produced through elastic DM-nucleon interactions. Within our model, such interactions can arise predominantly through the exchange of scalar states h and s , as well as interactions mediated by neutral gauge bosons Z and Z' . Moreover, the presence of the additional scalar S_1 provides a distinctive channel for such scatterings, thereby significantly affecting the phenomenology of direct detection constraints. The spin-independent DM nucleon scattering cross section, σ_{SIDD} , is predominantly controlled by the $U(1)_B$ symmetry-breaking scale v_B . Other model parameters, such as the mass splittings and Yukawa couplings, have subdominant effects. In our analysis, we focus on the effects of two input parameters on the obtained SIDD cross-section: v_B and Y_{S_1} . The parameter space for an obtained cross-section value is also used simultaneously to determine the DM relic abundance at that point, thereby identifying viable regions that meet both SIDD and relic requirements. As seen in the previous discussion, the obtained DM relic can be significantly affected by the strength of coannihilations via Ψ_2 , and thus the mass splitting $\Delta M(\Psi_2, \Psi_1)$ is also allowed to vary for the scans presented below. The fixed input parameters for these scans are chosen as $\lambda_S = 0.32$, $\lambda_{HS} = 1.29 \times 10^{-2}$, $\lambda_{S_1} = 10^{-2}$, $\lambda_{HS_1} = 10^{-4}$, $\lambda_{SS_1} = 10^{-10}$, $\sin \theta_{\text{DM}} = 0.001$, $m_s = 800$ GeV, and $m_{S_1} = 2$ TeV.

In Figure 5, we show the obtained results for the spin-independent DM-nucleon scattering cross section σ_{SIDD} as a function of the DM mass M_{DM} for two benchmark values of the fermion mass splitting, $\Delta M(\Psi_2, \Psi_1) = 10$ GeV (left column plots) and $\Delta M(\Psi_2, \Psi_1) = 1$ GeV (right column plots). The upper and lower rows correspond to two values for gauge coupling, $g_B = 0.01$ and $g_B = 0.05$, respectively. In each case, the Z' mass is varied within the range $M_{Z'} \in [500, 2000]$ GeV. Since $M_{Z'}$ is related to the $U(1)_B$ breaking scale by the relation given in Eq. (2.12), the scan over $M_{Z'}$ effectively corresponds to scanning over v_B for a given g_B . Therefore, the plot features in this figure arise from variations in v_B . From the plots, it can be observed that the obtained value of σ_{SIDD} depends on the value of $M_{Z'}$ and hence on v_B . We find that increasing v_B suppresses the effective DM-nucleon coupling, thereby reducing the DM-nucleon cross-section strength, σ_{SIDD} . This dependence explains the band-like regions obtained in all the plots in Figure 5 when $M_{Z'}$ is scanned over a range of $500 - 2000$ GeV. Additionally, the choice of mass splitting value plays a significant role in shaping the relic-density-allowed plot regions. For smaller splitting ($\Delta M(\Psi_2, \Psi_1) = 1$ GeV), efficient co-annihilation reduces the obtained relic density, leading to large under-abundant regions (orange colored). Conversely, for $\Delta M(\Psi_2, \Psi_1) = 10$ GeV, the co-annihilation strength is relatively weaker, resulting in more plot area under relic-favorable (blue colored) region. The apparent difference between the $g_B = 0.01$ (top row)

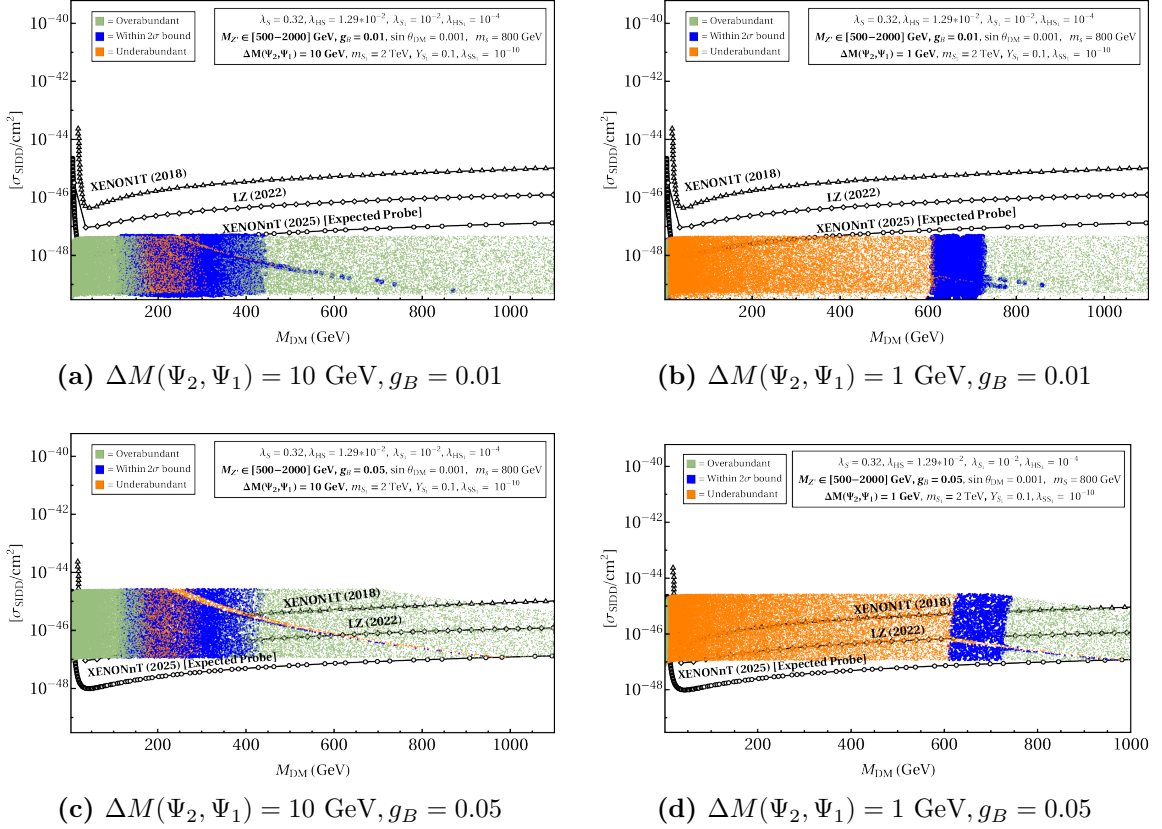


Figure 5: Spin-independent dark matter - nucleon scattering cross section σ_{SIDD} as a function of the dark matter mass M_{DM} for different benchmark scenarios. The top row corresponds to $M_{\text{DM}} = 10 \text{ GeV}$ with (a) $\Delta M(\Psi_2, \Psi_1) = 1 \text{ GeV}$ and (b) $\Delta M(\Psi_2, \Psi_1) = 10 \text{ GeV}$, while the bottom row corresponds to $M_{\text{DM}} = 1 \text{ GeV}$ with (c) $\Delta M(\Psi_2, \Psi_1) = 1 \text{ GeV}$ and (d) $\Delta M(\Psi_2, \Psi_1) = 10 \text{ GeV}$. In all cases, the fixed parameters are $\lambda_S = 0.32$, $\lambda_{HS} = 1.29 \times 10^{-2}$, $\lambda_{S_1} = 10^{-2}$, $\lambda_{HS_1} = 10^{-4}$, $\lambda_{SS_1} = 10^{-10}$, $\sin \theta_{\text{DM}} = 0.001$, $m_s = 800 \text{ GeV}$, $m_{S_1} = 2 \text{ TeV}$, and $Y_{S_1} = 0.1$. The Z' mass $M_{Z'}$ are varied within $M_{Z'} \in [500, 2000] \text{ GeV}$ with two fixed gauge coupling $g_B = 0.01, 0.05$, corresponding to different $U(1)_B$ breaking scales v_B . Current limits from XENON1T (2018) [71], LZ (2022) [70] and projected XENONnT (2025) [72] are also shown.

and $g_B = 0.05$ (bottom row) cases comes through the dependence of v_B on $M_{Z'}$ values for a given g_B . For larger g_B (bottom row), a given $M_{Z'}$ corresponds to a smaller v_B , which enhances the cross section, while for smaller g_B (top row) the corresponding v_B is larger, yielding smaller cross sections. In summary, the dominant effect in these plots originates from the variation of the breaking scale v_B (through the scan of $M_{Z'}$), while the mass splitting $\Delta M(\Psi_2, \Psi_1)$ determines the role of co-annihilations on the obtained DM relic values. The combined impact of v_B and $\Delta M(\Psi_2, \Psi_1)$ dictates which regions of the parameter space remain viable against the direct-detection limits from XENON1T(2018) [71], LZ(2022) [70] and under scrutiny from the expected data of XENONnT(2025) [72].

Similarly, Figure 6 illustrates the dependence of σ_{SIDD} on the Yukawa coupling, Y_{S_1} over a range $Y_{S_1} \in [0.001, 3]$. In this case, the obtained σ_{SIDD} remains essentially independent of the value of Y_{S_1} and thus thin horizontal plot lines color coded with the

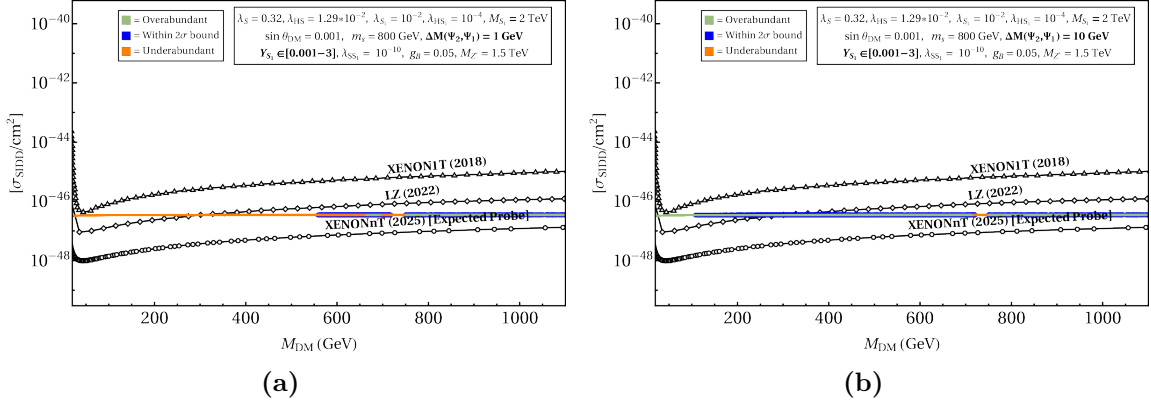


Figure 6: Spin-independent dark-matter-nucleon scattering cross section σ_{SIDD} as a function of the dark-matter mass M_{DM} . The results are shown for two benchmark choices of the input parameters: (a) $Y_{S_1} \in [0.001, 3]$ with $\Delta M(\Psi_2, \Psi_1) = 1 \text{ GeV}$, and (b) $Y_{S_1} \in [0.001, 3]$ with $\Delta M(\Psi_2, \Psi_1) = 10 \text{ GeV}$. The fixed parameters are $\lambda_S = 0.32$, $\lambda_{HS} = 1.29 \times 10^{-2}$, $\lambda_{S_1} = 10^{-2}$, $\lambda_{HS_1} = 10^{-4}$, $\lambda_{SS_1} = 10^{-10}$, $\sin \theta_{\text{DM}} = 0.001$, $m_s = 800 \text{ GeV}$, $m_{S_1} = 2 \text{ TeV}$, $g_B = 0.05$, and $M_{Z'} = 1.5 \text{ TeV}$. Current bounds from XENON1T (2018), LZ (2022), and the projected sensitivity of XENONnT (2025) are overlaid for comparison.

values of obtained DM relic as a function of $\Delta M(\Psi_2, \Psi_1)$ are obtained for both Figures 6a ($\Delta M(\Psi_2, \Psi_1) = 1 \text{ GeV}$) and 6b ($\Delta M(\Psi_2, \Psi_1) = 10 \text{ GeV}$). For given parameter space and input values, the obtained σ_{SIDD} is allowed from the LZ data for DM masses greater than 300 GeV, for both the plots. Additionally, for 6b, almost all the plot points allowed by the LZ data are also satisfied by the relic density requirements.

3.2 In-Direct Signatures

In this subsection, we focus on the detection of DM particles via their late-time annihilations into Standard Model particles, which can produce observable gamma rays. These processes may be observed in places where the DM density is still fairly high, yielding detectable signals from DM annihilations. Consequently, indirect detection efforts focus on identifying excess fluxes of such particles that cannot be attributed to known astrophysical processes, particularly in regions expected to host large DM densities, such as the Galactic center [73–75]. These observations may offer indirect evidence for DM through its annihilation channels. For a Dirac-type DM candidate (as considered in this work), the resulting gamma-ray spectrum typically consists of a broad continuum of final-state radiation (FSR). Due to the continuum nature of the spectrum, it is challenging to identify a distinct monoenergetic gamma-ray line. Consequently, in such scenarios, the predicted diffuse gamma-ray flux is usually compared with experimental observations rather than searching for sharp spectral features. In the plots below, we compute the expected diffuse gamma-ray flux from DM annihilation as a function of DM mass, accounting for the DM density distribution within the Galaxy. The presence of the Z' boson in the model introduces new late-time channels that lead to DM annihilations into SM final states. The Feynman diagrams corresponding to these Z' mediated processes are shown in the Appendix. The analysis

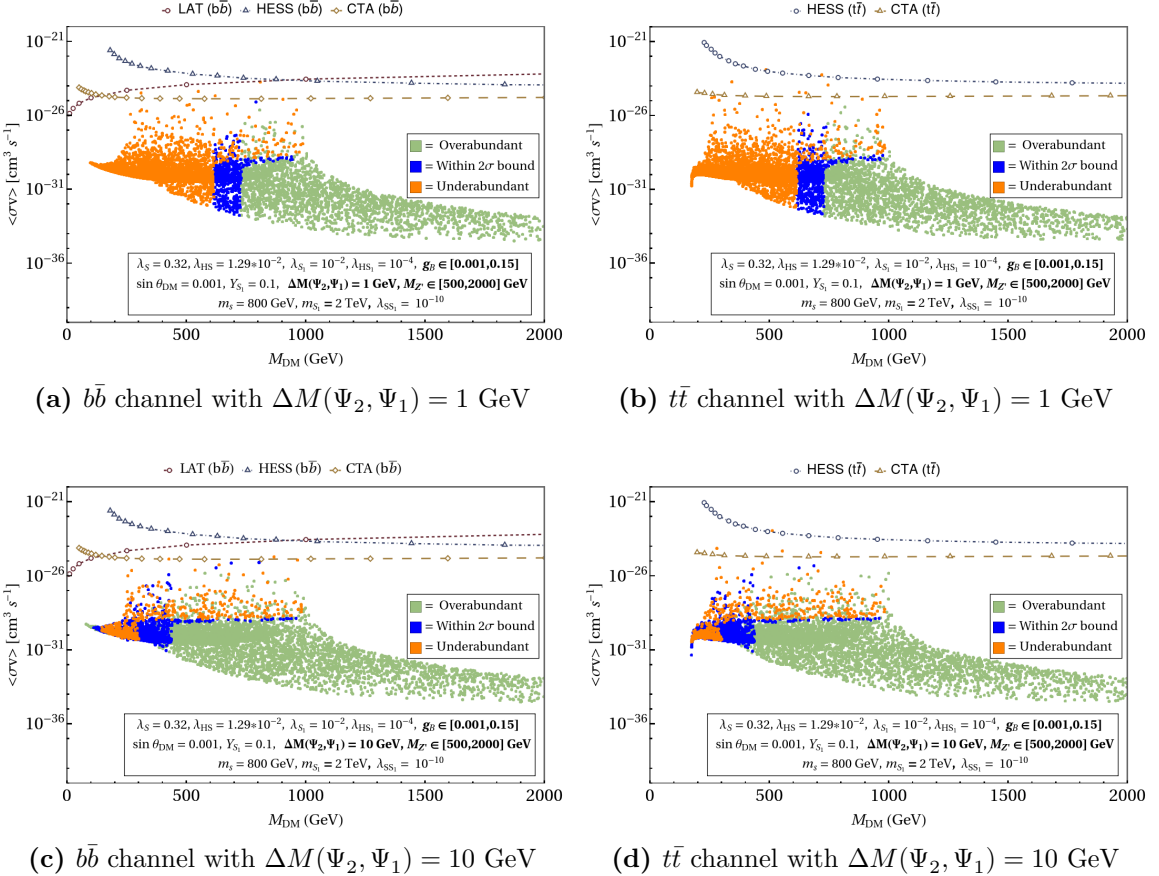


Figure 7: Thermally averaged annihilation cross section $\langle\sigma v\rangle$ as a function of the DM mass M_{DM} for two benchmark values $\Delta M(\Psi_2, \Psi_1) = 1 \text{ GeV}$ and 10 GeV , considering annihilation into $b\bar{b}$ and $t\bar{t}$ final states. The results are shown for varying $M_{Z'} \in [500, 2000]$ and $g_B \in [0.001, 0.15]$ corresponding to varying breaking scale v_B , while the relic-density allowed (blue), underabundant (orange), and overabundant (green) regions are indicated. Current indirect-detection bounds from LAT, HESS, and projected CTA sensitivities are also displayed for comparison.

specifically considers the dependence on the DM mass and relevant model parameters, such as the Yukawa coupling Y_{S_1} and the mass splitting $\Delta M(S_1, \Psi_1)$, which can modify the annihilation rates through co-annihilation or resonance effects. The predicted gamma-ray fluxes are then compared with current observational limits from Fermi-LAT [76, 77], HESS [78, 79] and CTA [80, 81], allowing us to identify regions of parameter space that are consistent with, or excluded by these astrophysical constraints. These signatures can serve as complementary probes to relic density requirements and direct detection constraints for the given DM candidate in our framework.

In Figure 7, we show the behavior of the velocity-averaged annihilation cross section $\langle\sigma v\rangle$ as a function of the dark-matter mass M_{DM} for two benchmark values of the mass splitting $\Delta M(\Psi_2, \Psi_1) = 1 \text{ GeV}$ (Figures 7a and 7b) and $\Delta M(\Psi_2, \Psi_1) = 10 \text{ GeV}$ (Figures 7c and 7d). The annihilation final states considered are the $b\bar{b}$ channel (Figures 7a and 7c) and the $t\bar{t}$ channel (Figures 7b and 7d). The input parameters are fixed to

$\lambda_S = 0.32$, $\lambda_{HS} = 1.29 \times 10^{-2}$, $\lambda_{S_1} = 10^{-2}$, $\lambda_{HS_1} = 10^{-4}$, $\lambda_{SS_1} = 10^{-10}$, $\sin \theta_{\text{DM}} = 0.001$, $m_s = 800$ GeV, $m_{S_1} = 2$ TeV, and $Y_{S_1} = 0.1$, while the gauge coupling and mediator mass are varied in the ranges $g_B \in [0.001, 0.15]$ and $M_{Z'} \in [500, 2000]$ GeV. Current bounds from LAT, HESS, and the projected sensitivity of CTA are also shown for comparison in the dashed line. We find that the blue points satisfying the observed relic density (within 2σ) typically yield annihilation cross sections below the current indirect-detection limits, though sizable regions remain testable in upcoming experiments for both $b\bar{b}$ and $t\bar{t}$ final states. Additionally, the dependence of the final DM relic on the coannihilations via Ψ_2 remains evident as we compare the results on top panel plots (where $\Delta M(\Psi_2, \Psi_1) = 1$ GeV) with the bottom panel plots (where $\Delta M(\Psi_2, \Psi_1) = 10$ GeV).

4 Flavor Physics Analysis

In this section, we investigate the impact of the baryonic gauge theory with a mixed-state DM sector on rare $b \rightarrow s\ell^+\ell^-$ transitions. The additional gauge interactions arising from the $U(1)_B$ symmetry, together with the mixing in the dark sector, induce the flavor-changing effects. These contributions can alter the theoretical predictions for semileptonic B meson decays and potentially explain deviations observed in current experimental data. To quantify these effects, we analyze the available measurements from exclusive decay channels, including $B \rightarrow (K^{(*)}, \phi) \ell^+\ell^-$, and use them to constrain the parameter space of the new physics interactions.

4.1 Effective Hamiltonian

The effective Hamiltonian governing the rare semileptonic $b \rightarrow s\ell^+\ell^-$ transition can be written as [82–84]

$$\mathcal{H}_{\text{eff}} = -\frac{4G_F}{\sqrt{2}} V_{tb} V_{ts}^* \left[C_7^{\text{eff}} \mathcal{O}_7 + C'_7 \mathcal{O}'_7 + \sum_{i=9,10,S,P} \left((C_i + C_i^{\text{NP}}) \mathcal{O}_i + C'_i \mathcal{O}'_i \right) \right], \quad (4.1)$$

where G_F is the Fermi constant and V_{ij} denote the CKM matrix elements. The local operators $\mathcal{O}_i^{(\prime)}$ encode the short-distance structure of the $b \rightarrow s\ell^+\ell^-$ interaction and are defined (for $\ell = \mu$) as

$$\begin{aligned} \mathcal{O}_7^{(\prime)} &= \frac{e}{16\pi^2} m_b (\bar{s}\sigma_{\mu\nu} P_{R(L)} b) F^{\mu\nu}, \\ \mathcal{O}_9^{(\prime)} &= \frac{e^2}{16\pi^2} (\bar{s}\gamma_\mu P_{L(R)} b) (\bar{\mu}\gamma^\mu \mu), \quad \mathcal{O}_{10}^{(\prime)} = \frac{e^2}{16\pi^2} (\bar{s}\gamma_\mu P_{L(R)} b) (\bar{\mu}\gamma^\mu \gamma_5 \mu), \\ \mathcal{O}_S^{(\prime)} &= \frac{e^2}{16\pi^2} m_b (\bar{s}P_{R(L)} b) (\bar{\mu}\mu), \quad \mathcal{O}_P^{(\prime)} = \frac{e^2}{16\pi^2} m_b (\bar{s}P_{R(L)} b) (\bar{\mu}\gamma_5 \mu). \end{aligned}$$

Here, $P_{L,R} = (1 \mp \gamma_5)/2$ are the chirality projection operators, and the Wilson coefficients $C_i^{(\prime)}$ parametrize the corresponding short-distance interactions. Within the Standard Model, only the unprimed vector and axial-vector operators contribute, while the primed and (pseudo)scalar operators arise solely from physics beyond it.

4.2 The $b \rightarrow s\ell^+\ell^-$ decay observables

The rare semileptonic decay $B \rightarrow K\ell^+\ell^-$ is mediated by the flavor-changing neutral current transition $b \rightarrow s\ell^+\ell^-$, which is loop-suppressed in the Standard Model. Owing to its relatively simple hadronic structure, this channel provides a theoretically clean environment for probing short-distance dynamics. In the Standard Model, the q^2 -dependent differential branching ratio can be expressed as [85]

$$\frac{d\mathcal{BR}}{dq^2} = \tau_{B_c} \left(2a_\ell + \frac{2}{3}c_\ell \right), \quad (4.2)$$

where the quantities a_ℓ and c_ℓ encode the dynamical information about the decay and are defined as

$$a_\ell = \frac{G_F^2 \alpha_{EW}^2 |V_{tb} V_{ts}^*|^2}{2^9 \pi^5 m_B^3} \beta_\ell \sqrt{\lambda} \left[q^2 |F_P|^2 + \frac{\lambda}{4} (|F_A|^2 + |F_V|^2) + 4m_\ell^2 m_B^2 |F_A|^2 + 2m_\ell (m_B^2 - m_K^2 + q^2) \text{Re}(F_P F_A^*) \right], \quad (4.3)$$

$$c_\ell = -\frac{G_F^2 \alpha_{EW}^2 |V_{tb} V_{ts}^*|^2}{2^9 \pi^5 m_B^3} \beta_\ell \sqrt{\lambda} \frac{\lambda \beta_\ell^2}{4} (|F_A|^2 + |F_V|^2). \quad (4.4)$$

The parameter λ , and the lepton mass factor β_ℓ appearing above are given by

$$\lambda = q^4 + m_B^4 + m_K^4 - 2(m_B^2 m_K^2 + m_B^2 q^2 + m_K^2 q^2), \quad (4.5)$$

$$\beta_\ell = \sqrt{1 - \frac{4m_\ell^2}{q^2}}. \quad (4.6)$$

The hadronic dynamics are encoded in the parameters F_P , F_V , and F_A , which can be written in terms of the short-distance Wilson coefficients and the $B \rightarrow K$ transition form factors as

$$F_P = -m_\ell C_{10} \left[f_+ - \frac{m_{B_c}^2 - m_{D_s}^2}{q^2} (f_0 - f_+) \right], \quad (4.7)$$

$$F_V = C_9^{\text{eff}} f_+ + \frac{2m_b}{m_{B_c} + m_{D_s}} C_7^{\text{eff}} f_T, \quad (4.8)$$

$$F_A = C_{10} f_+. \quad (4.9)$$

For the vector final state, the decay amplitude of $B \rightarrow (K^*, \phi) \ell^+\ell^-$ can be derived from the effective Hamiltonian given in Eq. (4.1). The corresponding differential branching ratios read [86]

$$\frac{d\mathcal{BR}}{dq^2} = \frac{1}{4} \tau_B [3I_1^c + 6I_1^s - I_2^c - 2I_2^s], \quad (4.10)$$

where the angular coefficients I_i depend on q^2 and are listed in Appendix B.2.

In addition to the branching ratio, several angular observables provide valuable probes of the underlying dynamics. Among these, we consider the forward-backward asymmetry

A_{FB} and the longitudinal polarization fraction F_L , defined as [43]

$$F_L(q^2) = \frac{3I_1^c - I_2^c}{3I_1^c + 6I_1^s - I_2^c - 2I_2^s}, \quad A_{FB}(q^2) = \frac{3I_6}{3I_1^c + 6I_1^s - I_2^c - 2I_2^s}. \quad (4.11)$$

Another set of notable observables are the six form-factor-independent (FFI) observables [43], which are defined as

$$\begin{aligned} \langle P_1 \rangle &= \frac{\int_{\text{bin}} dq^2 I_3}{2 \int_{\text{bin}} dq^2 I_{2s}}, & \langle P_2 \rangle &= \frac{\int_{\text{bin}} dq^2 I_6}{8 \int_{\text{bin}} dq^2 I_{2s}}, \\ \langle P_3 \rangle &= -\frac{\int_{\text{bin}} dq^2 I_9}{4 \int_{\text{bin}} dq^2 I_{2s}}, & \langle P_4 \rangle &= \frac{\int_{\text{bin}} dq^2 \sqrt{2} I_4}{\sqrt{-\int_{\text{bin}} dq^2 I_2^c \int_{\text{bin}} dq^2 (2I_{2s} - I_3)}}, \\ \langle P_5 \rangle &= \frac{\int_{\text{bin}} dq^2 I_5}{\sqrt{-\int_{\text{bin}} dq^2 2I_2^c \int_{\text{bin}} dq^2 (2I_{2s} + I_3)}}, & \langle P_6 \rangle &= -\frac{\int_{\text{bin}} dq^2 I_7}{\sqrt{-\int_{\text{bin}} dq^2 2I_2^c \int_{\text{bin}} dq^2 (2I_{2s} - I_3)}}. \end{aligned} \quad (4.12)$$

A modified set of optimized clean observables P'_4, P'_5, P'_6 can also be defined, which are related to the original observables via [43]

$$\langle P'_4 \rangle = \frac{\int_{\text{bin}} dq^2 I_4}{2 \sqrt{-\int_{\text{bin}} dq^2 I_2^c \int_{\text{bin}} dq^2 I_2^s}}, \quad \langle P'_5 \rangle = \frac{\int_{\text{bin}} dq^2 I_5}{2 \sqrt{-\int_{\text{bin}} dq^2 I_2^c \int_{\text{bin}} dq^2 I_2^s}}, \quad (4.13)$$

$$\langle P'_6 \rangle = -\frac{\int_{\text{bin}} dq^2 I_7}{2 \sqrt{-\int_{\text{bin}} dq^2 I_2^c \int_{\text{bin}} dq^2 I_2^s}}, \quad \langle P'_8 \rangle = -\frac{\int_{\text{bin}} dq^2 I_8}{2 \sqrt{-\int_{\text{bin}} dq^2 I_2^c \int_{\text{bin}} dq^2 I_2^s}}. \quad (4.14)$$

These clean observables are particularly useful as they reduce dependence on hadronic form factors, making them robust probes for testing the Standard Model predictions and exploring potential new physics effects. To probe lepton flavor universality (LFU), one can define observables that directly compare the muon and electron final states. In particular, the quantities $\langle Q_4 \rangle$ and $\langle Q_5 \rangle$ are given by [41, 87]

$$\langle Q_4 \rangle = \langle P'_4^\mu \rangle - \langle P'_4^e \rangle, \quad \langle Q_5 \rangle = \langle P'_5^\mu \rangle - \langle P'_5^e \rangle. \quad (4.15)$$

Finally, the ratio of branching fractions between the muon and electron modes for $B \rightarrow K^{(*)}\ell^+\ell^-$ decays are given as

$$R_{K^{(*)}}(q^2) = \frac{\mathcal{BR}(B \rightarrow K^{(*)}\mu^+\mu^-)}{\mathcal{BR}(B \rightarrow K^{(*)}e^+e^-)}. \quad (4.16)$$

The measurement of these observables allows comparisons with the SM contributions and can reveal possible new physics in $b \rightarrow s\mu^+\mu^-$ transition decays. Using the above-discussed observables, we constrain the allowed new physics parameters to the relevant Wilson coefficients, which are analyzed below.

4.3 Constraint on new physics parameters from $b \rightarrow s\mu^+\mu^-$ transitions

Motivated by the persistent anomalies reported in semileptonic $b \rightarrow s\mu^+\mu^-$ transitions, we investigate possible contributions arising from the scalar-assisted baryonic gauge framework. Our analysis focuses on the set of observables that exhibit statistically significant deviations from their SM expectations and are therefore particularly sensitive to potential new physics effects. Within this setup, the new physics contributions are obtained in the vector and axial-vector Wilson coefficients C_9^{NP} and C_{10}^{NP} governing the short-distance dynamics of $b \rightarrow s\mu^+\mu^-$ processes. Accordingly, we explore the viable regions of parameter space for the new physics encoded in these coefficients. For this analysis, the complete set of $b \rightarrow s\mu^+\mu^-$ observables employed in the fit is summarized below.

- **$b \rightarrow s\mu^+\mu^-$ observables without lepton flavor universality**

We include a comprehensive set of observables induced by the $b \rightarrow s\mu^+\mu^-$ transition. In particular, we use the latest LHCb measurement of the branching ratio \mathcal{B} ($B_s \rightarrow \mu^+\mu^-$) reported at Moriond 2021 [88], which is consistent with earlier combined results from ATLAS, CMS, and LHCb [89–91]. We further incorporate the branching ratios of $B \rightarrow K^{(*)}\mu^+\mu^-$ [49, 92] and $B_s \rightarrow \phi\mu^+\mu^-$ [51], measured in different q^2 bins. Additionally, the angular observables are also taken into account. These include the forward-backward asymmetry A_{FB} , the longitudinal polarization fraction F_L , and the optimized observables P_1 - P'_8 measured in $B^{0(+)} \rightarrow K^{*0(+)}\mu^+\mu^-$ decays by LHCb [42, 93, 94]. We also include the measurement of F_L in $B_s \rightarrow \phi\mu^+\mu^-$ [95].

- **Lepton flavor universality sensitive observables**

To test lepton flavor universality, we include the LHCb measurements of the ratios $R_{K_S^0}$ and $R_{K^{*+}}$ [38], together with the updated results for $R_{K^{(*)}}$ [37]. We also consider the Belle measurements of the optimized differences $\langle Q_4 \rangle$ and $\langle Q_5 \rangle$ [96], which provide additional sensitivity to non-universal new physics effects.

In this study, we employ all the observables discussed above and conduct our analysis using the `flavio` package [39].

Now in the presence of new physics, the exclusive processes mediated by $b \rightarrow s\mu^+\mu^-$ transitions receive additional contributions beyond the SM. The vertices arise from new interactions, including those associated with the baryonic gauge sector and the mixed-state DM field. These rare transitions receive non-zero contributions at the one-loop level and are shown in Figure 8. The effects can eventually be parametrized in terms of modified Wilson coefficients. These couplings include the exchange of the neutral gauge boson Z' , Z , γ as well as the scalar states $H_{1,2}$, with scalar field S_1 and fermions $\psi_{1,2}$ propagating inside the loop, as illustrated in Figure 8. The penguin diagram in the bottom-left panel is suppressed by the factor $m_b/M_{\psi_{1,2}}$, thus providing a negligible contribution. The loop functions associated with the Higgs contribution are suppressed by factors of $m_q M_{\psi_{1,2}}/m_{S_1}^2$ and therefore yield numerically negligible effects. Therefore, the Higgs-mediated effects, depicted in the bottom panel, are omitted. On the other hand, the new neutral gauge boson Z' can generate flavor-changing effects at the quark level through loop-induced penguin

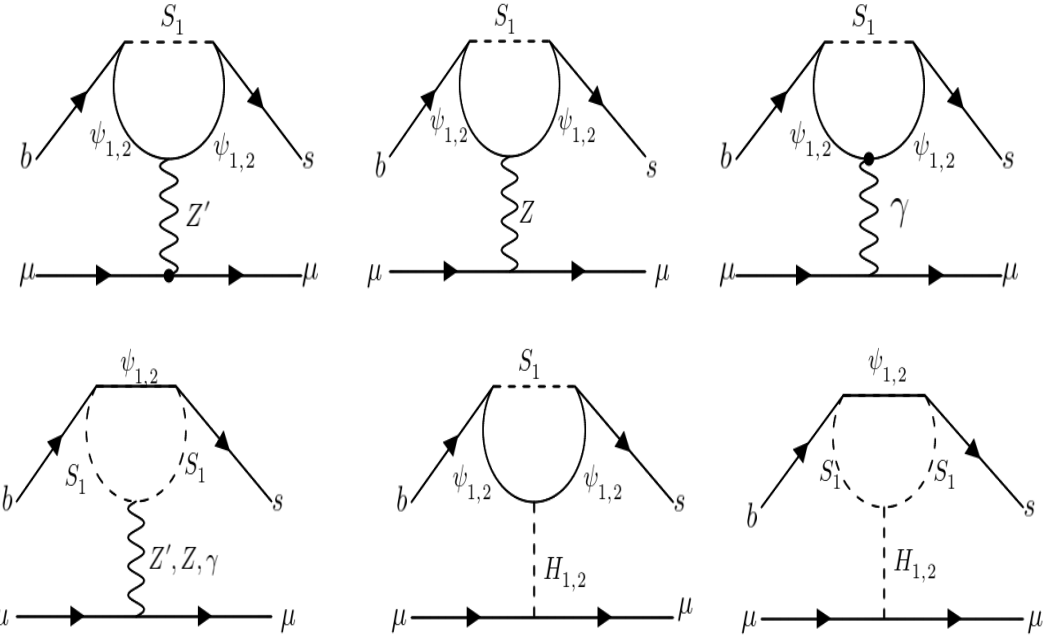


Figure 8: Allowed penguin diagrams illustrating the $b \rightarrow s\mu^+\mu^-$ transition.

diagrams. Although its couplings to charged leptons are suppressed, the corresponding Z' contribution is retained for completeness. In addition, the loop-induced penguin diagrams mediated by the SM Z boson and the photon provide relevant contributions to the effective $b \rightarrow s\ell^+\ell^-$ operators. This is due to the presence of an electroweak doublet component and also the presence of the hypercharge in the DM candidate, which induces the couplings to these gauge bosons. Therefore, our analysis includes the Z , Z' , and γ penguin contributions shown in the top panel. On the other hand, the γ -penguin diagrams generate effective $b \rightarrow s\ell^+\ell^-$ interactions through vector and electromagnetic dipole operators. Consequently, no axial–vector operator is induced with the coefficient C_{10}^{NP} , and it remains unaffected by the photon exchange. So the contribution associated with the photon is restricted to the Wilson coefficients C_9^{NP} and C_7^{NP} . However, the C_7^{NP} contribution includes a factor of m_s . So, we have neglected this contribution in our analysis.

Now, in the presence of Z' , Z and γ exchanging one loop diagram, the transition amplitudes of semileptonic $b \rightarrow s\ell^+\ell^-$ decay process is given as

$$\begin{aligned} \mathcal{M}_{Z'-\psi} = & -\frac{1}{(4\pi)^2} (0.015) Y_{S_1}^2 \frac{\mathcal{R}_{Z'-\psi}(a, b)}{M_{Z'}^2} [\bar{s}(p') \gamma^\mu P_L b(p)] [\bar{\ell}(q_2) \gamma_\mu \ell(q_1)] \\ & + \frac{1}{(4\pi)^2} (0.008) Y_{S_1}^2 \frac{\mathcal{R}_{Z'-\psi}(a, b)}{M_{Z'}^2} [\bar{s}(p') \gamma^\mu P_L b(p)] [\bar{\ell}(q_2) \gamma_\mu \gamma_5 \ell(q_1)] \end{aligned} \quad (4.17)$$

$$\begin{aligned}\mathcal{M}_{Z-\psi} = & -\frac{1}{(4\pi)^2} Y_{S_1}^2(0.020) \frac{\mathcal{R}_{Z'-\psi}(a, b)}{M_{Z'}^2} [\bar{s}(p') \gamma^\mu P_L b(p)] [\bar{\ell}(q_2) \gamma_\mu \ell(q_1)] \\ & + \frac{1}{(4\pi)^2} Y_{S_1}^2(0.015) \frac{\mathcal{R}_{Z'-\psi}(a, b)}{M_{Z'}^2} [\bar{s}(p') \gamma^\mu P_L b(p)] [\bar{\ell}(q_2) \gamma_\mu \gamma_5 \ell(q_1)]\end{aligned}\quad (4.18)$$

$$\mathcal{M}_{\gamma-\psi} = -\frac{1}{(4\pi)^2} Y_{S_1}^2(0.5) \frac{\mathcal{R}_{Z'-\psi}(a, b)}{M_{Z'}^2} [\bar{s}(p') \gamma^\mu P_L b(p)] [\bar{\ell}(q_2) \gamma_\mu \ell(q_1)] \quad (4.19)$$

which, in comparison with the generalized effective Hamiltonian, provides additional new Wilson coefficients as

$$C_9^{NP, Z'-\psi} = -\frac{1}{4\pi} \frac{\sqrt{2}}{4G_F M_{Z'}^2} (0.015) \frac{1}{\alpha_{em}} \frac{Y_{S_1}^2}{V_{tb} V_{ts}^*} \mathcal{R}_{Z'-\psi}(a, b), \quad (4.20)$$

$$C_9^{NP, Z-\psi} = -\frac{1}{4\pi} \frac{\sqrt{2}}{4G_F M_{Z'}^2} (0.020) \frac{1}{\alpha_{em}} \frac{Y_{S_1}^2}{V_{tb} V_{ts}^*} \mathcal{R}_{Z-\psi}(a, b), \quad (4.21)$$

$$C_9^{NP, \gamma-\psi} = -\frac{1}{4\pi} \frac{\sqrt{2}}{4G_F M_{Z'}^2} (0.5) \frac{1}{\alpha_{em}} \frac{Y_{S_1}^2}{V_{tb} V_{ts}^*} \mathcal{R}_{\gamma-\psi}(a, b). \quad (4.22)$$

and

$$C_{10}^{NP, Z'-\psi} = \frac{1}{4\pi} \frac{\sqrt{2}}{4G_F M_{Z'}^2} (0.008) \frac{1}{\alpha_{em}} \frac{Y_{S_1}^2}{V_{tb} V_{ts}^*} \mathcal{R}_{Z'-\psi}(a, b), \quad (4.23)$$

$$C_{10}^{NP, Z-\psi} = \frac{1}{4\pi} \frac{\sqrt{2}}{4G_F M_{Z'}^2} (0.015) \frac{1}{\alpha_{em}} \frac{Y_{S_1}^2}{V_{tb} V_{ts}^*} \mathcal{R}_{Z-\psi}(a, b) \quad (4.24)$$

where the loop functions are given as

$$\begin{aligned}\mathcal{R}_{Z'-\psi}(a, b) = & \left[\sin^2 \theta_{\text{DM}} \left\{ \left(g_B \cos^2 \theta_{\text{DM}} - \frac{3}{2} g_B \cos 2\theta_{\text{DM}} + 0.017 \sin^2 \theta_{\text{DM}} \right) \right. \right. \\ & \times \left(\frac{1}{8} - \frac{5a^2 - 8a + 3 - 2a^2 \ln a}{8(a-1)^2} \right) + \left(0.5g_B + 0.00028 + g_B \cos^2 \theta_{\text{DM}} \right) \\ & \times \left. \left(\frac{1}{8} + \frac{-3 + 3a^2 - 8a \ln a + 2a^2 \ln a}{8(a-1)^2} \right) \right\} \\ & + \cos^2 \theta_{\text{DM}} \left\{ \left(-g_B \sin^2 \theta_{\text{DM}} - \frac{3}{2} g_B \cos 2\theta_{\text{DM}} - 0.017 \sin^2 \theta_{\text{DM}} - 0.017 \cos 2\theta_{\text{DM}} \right) \right. \\ & \times \left(\frac{1}{8} - \frac{5b^2 - 8b + 3 - 2b^2 \ln b}{8(b-1)^2} \right) + \left(-\frac{3}{2}g_B + 0.00028 \right) \\ & \times \left. \left(\frac{1}{8} + \frac{-3 + 3b^2 - 8b \ln b + 2b^2 \ln b}{8(b-1)^2} \right) \right\} \right]. \quad (4.25)\end{aligned}$$

$$\begin{aligned}
\mathcal{R}_{Z-\psi}(a, b) = & \left[\sin^2 \theta_{\text{DM}} \left\{ \left(0.005 \cos 2\theta_{\text{DM}} - 0.366 \sin^2 \theta_{\text{DM}} \right) \right. \right. \\
& \times \left(\frac{1}{8} - \frac{5a^2 - 8a + 3 - 2a^2 \ln a}{8(a-1)^2} \right) + \left(0.020g_B - 0.014 + 0.005 \sin^2 \theta_{\text{DM}} \right) \\
& \times \left. \left(\frac{1}{8} + \frac{-3 + 3a^2 - 8a \ln a + 2a^2 \ln a}{8(a-1)^2} \right) \right\} \\
& + \cos^2 \theta_{\text{DM}} \left\{ \left(0.371 \cos 2\theta_{\text{DM}} + 0.376 \sin^2 \theta_{\text{DM}} \right) \right. \\
& \times \left(\frac{1}{8} - \frac{5b^2 - 8b + 3 - 2b^2 \ln b}{8(b-1)^2} \right) + \left(0.01 \cos 2\theta_{\text{DM}} - 0.02g_B + 0.024 \sin^2 \theta_{\text{DM}} \right) \\
& \times \left. \left. \left(\frac{1}{8} + \frac{-3 + 3b^2 - 8b \ln b + 2b^2 \ln b}{8(b-1)^2} \right) \right\} \right]. \tag{4.26}
\end{aligned}$$

$$\begin{aligned}
\mathcal{R}_{\gamma-\psi}(a, b) = & \left[\sin^2 \theta_{\text{DM}} \left\{ \left(g_B \cos^2 \theta_{\text{DM}} - \frac{3}{2}g_B \cos 2\theta_{\text{DM}} + 0.017 \sin^2 \theta_{\text{DM}} \right) \right. \right. \\
& \times \left(\frac{1}{8} - \frac{5a^2 - 8a + 3 - 2a^2 \ln a}{8(a-1)^2} \right) + \left(0.5g_B + 0.00028 + g_B \cos^2 \theta_{\text{DM}} \right) \\
& \times \left. \left(\frac{1}{8} + \frac{-3 + 3a^2 - 8a \ln a + 2a^2 \ln a}{8(a-1)^2} \right) \right\} \\
& + \cos^2 \theta_{\text{DM}} \left\{ \left(-g_B \sin^2 \theta_{\text{DM}} - \frac{3}{2}g_B \cos 2\theta_{\text{DM}} - 0.017 \sin^2 \theta_{\text{DM}} - 0.017 \cos 2\theta_{\text{DM}} \right) \right. \\
& \times \left(\frac{1}{8} - \frac{5b^2 - 8b + 3 - 2b^2 \ln b}{8(b-1)^2} \right) + \left(-\frac{3}{2}g_B + 0.00028 \right) \\
& \times \left. \left. \left(\frac{1}{8} + \frac{-3 + 3b^2 - 8b \ln b + 2b^2 \ln b}{8(b-1)^2} \right) \right\} \right] \tag{4.27}
\end{aligned}$$

with

$$a = \frac{M_{\psi_1}^2}{m_{S_1}^2}, \quad b = \frac{M_{\psi_2}^2}{m_{S_1}^2}. \tag{4.28}$$

Now,

$$C_9^{\text{NP}} = C_9^{\text{NP}, Z'-\psi} + C_9^{\text{NP}, Z-\psi} + C_9^{\text{NP}, \gamma-\psi}, \tag{4.29}$$

$$C_{10}^{\text{NP}} = C_{10}^{\text{NP}, Z'-\psi} + C_{10}^{\text{NP}, Z-\psi}. \tag{4.30}$$

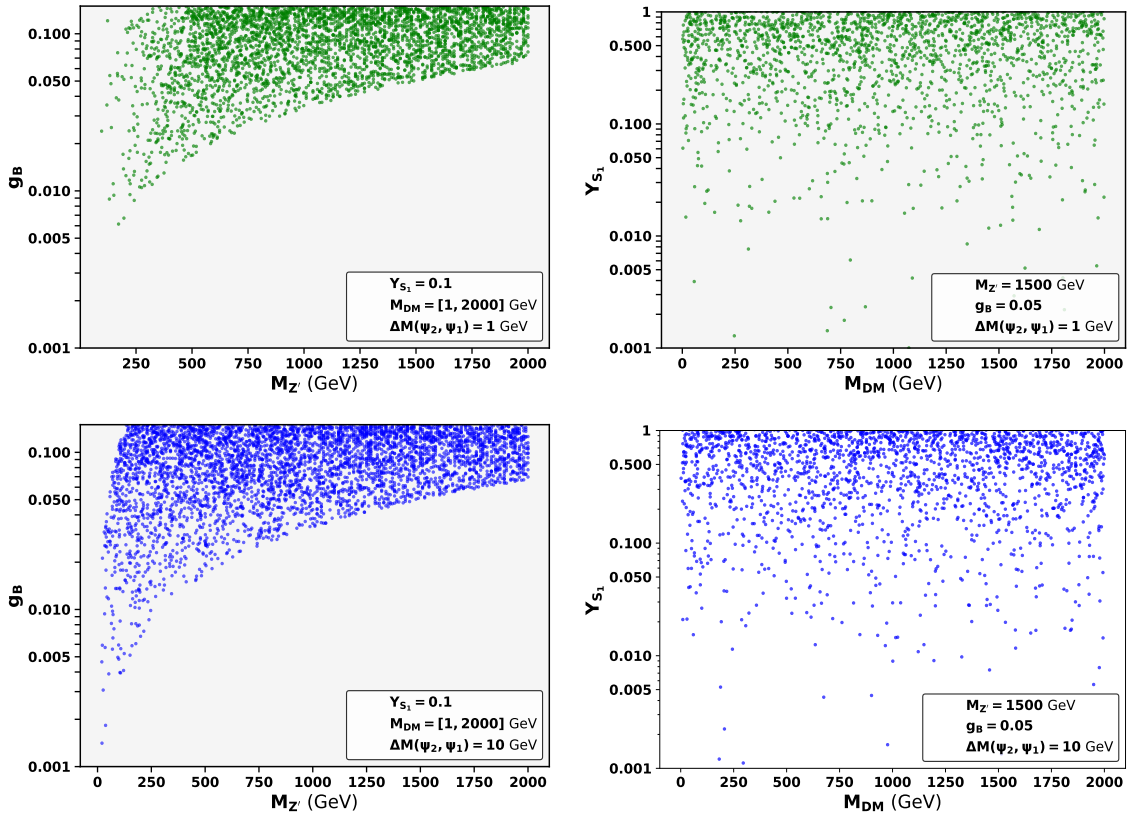


Figure 9: Allowed parameter space in the $U(1)_B$ model. **Top-left panel:** $U(1)_B$ gauge coupling g_B versus Z' mass $M_{Z'}$, **Top-right panel:** Yukawa coupling Y_{S_1} versus DM mass M_{DM} for a mass splitting $\Delta M(\Psi_2, \Psi_1) = 1$ GeV. Bottom panel: Same as top, but for $\Delta M(\Psi_2, \Psi_1) = 10$ GeV, illustrating the impact of $\Delta M(\Psi_2, \Psi_1)$ on the allowed region. Legends show benchmark values used in the scans, $M_{Z'} = 1500$ GeV, $g_B = 0.05$, $Y_{S_1} = 0.1$ and $\Delta M(\Psi_2, \Psi_1) = 1$ or 10 GeV.

Having established the structure of the new physics contributions to the Wilson coefficients, we now discuss the viable domain arising from the parameters g_B , Y_{S_1} , $M_{Z'}$, and $M_{\psi_{1,2}}$. In our model, we assume the lighter ψ_1 particle to be DM, and denote its mass as M_{DM} . Figure 9 illustrates the allowed regions of the parameter space after incorporating all relevant phenomenological constraints. In the top-left panel, the correlation between the $U(1)_B$ gauge coupling g_B and the Z' boson mass $M_{Z'}$ is shown, indicating that larger gauge couplings require heavier mediator masses in order to remain consistent with experimental bounds. This behavior reflects the sensitivity of flavor observables and indirect searches to the strength of the new gauge interaction. On the other hand, the top-right panel shows the viable allowed region in the Y_{S_1} - M_{DM} plane for a small mass splitting $\Delta M(\Psi_2, \Psi_1) = 1$ GeV. In this nearly degenerate regime, the allowed region is relatively broad, indicating a mild dependence on the DM mass for moderate values of the Yukawa coupling. In contrast, the bottom panel shows that increasing the mass splitting to $\Delta M(\Psi_2, \Psi_1) = 10$ GeV leads to a notable modification of the allowed region. This

highlights the important role played by the dark sector mass hierarchy in shaping the phenomenology of the model. Overall, these results emphasize that the interplay between the gauge sector, the Yukawa interactions, and the dark-sector mass spectrum imposes nontrivial constraints on the parameter space of the $U(1)_B$ model.

5 Summarized discussion: Combined Flavor and DM Analysis

The simultaneous study of flavor physics and DM phenomenology is crucial for establishing a consistent new physics framework. In the present model, the same set of parameters that governs the interactions of the dark sector also enters the physics associated with the $b \rightarrow s\mu^+\mu^-$ transitions. As a result, constraints from the flavor sector restrict the viable parameter space of the dark sector, and vice versa. Therefore, a combined analysis goes beyond treating flavor physics and DM as independent probes. This approach allows us to identify regions of the parameter space that are simultaneously compatible with the flavor anomalies and DM constraints, thereby providing a robust test of the underlying new physics. To this end, we perform a combined numerical scan of the relevant parameter space consistent with both DM and flavor phenomenology and present our results in Figs. 10 and 11.

$\lambda_S = 0.32, \lambda_{HS} = 1.29 \times 10^{-2}, \lambda_{S_1} = 10^{-2}, \lambda_{HS_1} = 10^{-4}, \lambda_{SS_1} = 10^{-10}$ $\sin \theta_{\text{DM}} = 0.001, m_S = 800 \text{ GeV}, m_{S_1} = 2 \text{ TeV}, Y_{S_1} = 0.1$									
$\Delta M(\Psi_2, \Psi_1) = 1 \text{ GeV}$					$\Delta M(\Psi_2, \Psi_1) = 10 \text{ GeV}$				
g_B	$M_{Z'}$ (GeV)	M_{DM} (GeV)	Ωh^2	$\sigma_{\text{SIDD/cm}^2}$	g_B	$M_{Z'}$ (GeV)	M_{DM} (GeV)	Ωh^2	$\sigma_{\text{SIDD/cm}^2}$
0.0493	1145.8	535.4	0.117	9.53×10^{-47}	0.0600	1575.5	617.8	0.097	5.86×10^{-47}
0.0481	1625.9	784.7	0.095	2.19×10^{-47}	0.0537	1395.8	610.9	0.095	6.11×10^{-47}
0.0459	1374.0	649.3	0.126	3.54×10^{-47}	0.0660	1711.3	607.8	0.094	6.16×10^{-47}
0.0487	1255.3	592.3	0.11	6.36×10^{-47}	0.0410	1148.8	658.1	0.11	4.56×10^{-47}
0.0481	1722.8	828.4	0.114	1.75×10^{-47}	0.0604	1674.1	651.9	0.11	4.79×10^{-47}
0.0470	1897.19	918.52	0.11	1.10×10^{-47}	0.0399	1045.32	615.21	0.095	5.96×10^{-47}
0.0485	1443.17	688.32	0.1112	3.58×10^{-47}	0.0229	600.49	617.21	0.095	5.92×10^{-47}
0.0490	1311.16	620.08	0.114	5.47×10^{-47}	0.0288	754.83	616.60	0.095	5.92×10^{-47}
0.0484	1133.79	531.17	0.11	9.27×10^{-47}	0.0462	1295.61	658.02	0.11	4.55×10^{-47}
0.0481	1518.22	725.75	0.115	2.84×10^{-47}	0.0282	733.04	610.56	0.095	6.08×10^{-47}

Table 2: Randomly selected allowed points in the $(g_B, M_{Z'})$ plane for $\Delta M(\Psi_2, \Psi_1) = 1 \text{ GeV}$ (**left side**) and $\Delta M(\Psi_2, \Psi_1) = 10 \text{ GeV}$ (**right side**). For each allowed point, the corresponding DM mass is also listed in the table. These points satisfy the relic density constraint within 2σ , are consistent with SIDD bounds from LZ (2022), and are allowed by Flavor physics constraints as shown in Figure 10.

In Figure 10, we observe that the overall allowed region (pink colored) is significantly restricted once both flavor and DM constraints are imposed. Additionally, on comparing the **Top Panel** with the **Bottom Panel**, we observe that increasing the mass splitting $\Delta M(\Psi_2, \Psi_1)$ leads to a noticeable reduction of the viable parameter space in the g_B - $M_{Z'}$ plane. This is due to the increased co-annihilation efficiency assisted via the next-to-lightest state Ψ_2 , which drives the final DM relic to be under-abundant for a vast region of parameter space.

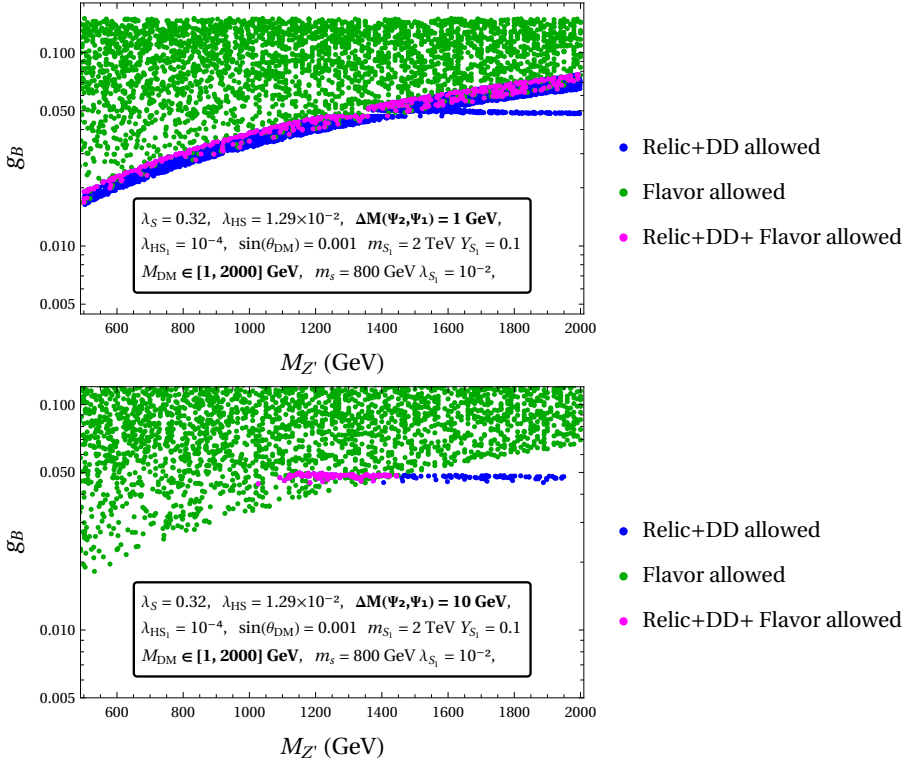


Figure 10: Allowed common parameter space in the plane of $M_{Z'} - g_B$ from both DM and flavor phenomenology for **Top Panel:** $\Delta M(\Psi_2, \Psi_1) = 1$ GeV and **Bottom Panel:** $\Delta M(\Psi_2, \Psi_1) = 10$ GeV, with fixed parameters: $\lambda_S = 0.32$, $\lambda_{HS} = 1.29 \times 10^{-2}$, $\lambda_{S_1} = 10^{-2}$, $\lambda_{HS_1} = 10^{-4}$, $\sin \theta_{DM} = 0.001$, $m_s = 800$ GeV, $m_{S_1} = 2$ TeV. The DM mass is varied between 1 to 2000 GeV.

$\lambda_S = 0.32, \lambda_{HS} = 1.29 \times 10^{-2}, \lambda_{S_1} = 10^{-2}, \lambda_{HS_1} = 10^{-4}, \lambda_{SS_1} = 10^{-10}$ $\sin \theta_{DM} = 0.001, m_s = 800$ GeV, $M_{Z'} = 1.5$ TeV, $g_B = 0.05$.							
$\Delta M(\Psi_2, \Psi_1) = 1$ GeV				$\Delta M(\Psi_2, \Psi_1) = 10$ GeV			
Y_{S_1}	M_{DM} (GeV)	Ωh^2	σ_{SIDD/cm^2}	Y_{S_1}	M_{DM} (GeV)	Ωh^2	σ_{SIDD/cm^2}
0.0797	674.79	0.1101	3.51×10^{-47}	0.4254	159.45	0.112	3.44×10^{-47}
0.9543	1793.22	0.0987	3.53×10^{-47}	0.4898	259.44	0.1035	3.46×10^{-47}
0.1589	677.13	0.1124	3.49×10^{-47}	0.0970	383.61	0.1261	3.47×10^{-47}
0.1941	632.72	0.1021	3.47×10^{-47}	0.1289	419.87	0.121	3.49×10^{-47}
1.0759	634.56	0.1009	3.47×10^{-47}	1.5315	532.94	0.114	3.48×10^{-47}
0.9378	1324.62	0.1213	3.51×10^{-47}	1.4103	630.81	0.115	3.48×10^{-47}
1.0553	1056.21	0.0943	3.51×10^{-47}	1.2124	842.73	0.123	3.49×10^{-47}
0.2830	680.52	0.1170	3.48×10^{-47}	1.0605	1266.29	0.117	3.51×10^{-47}
0.1244	615.18	0.0959	3.47×10^{-47}	1.0062	1666.16	0.111	3.52×10^{-47}
0.4452	713.68	0.1005	3.49×10^{-47}	0.999	1994.89	0.120	3.68×10^{-47}

Table 3: Similar to Table 2, but in the plane of $M_{DM} - Y_{S_1}$ as shown in Figure 11.

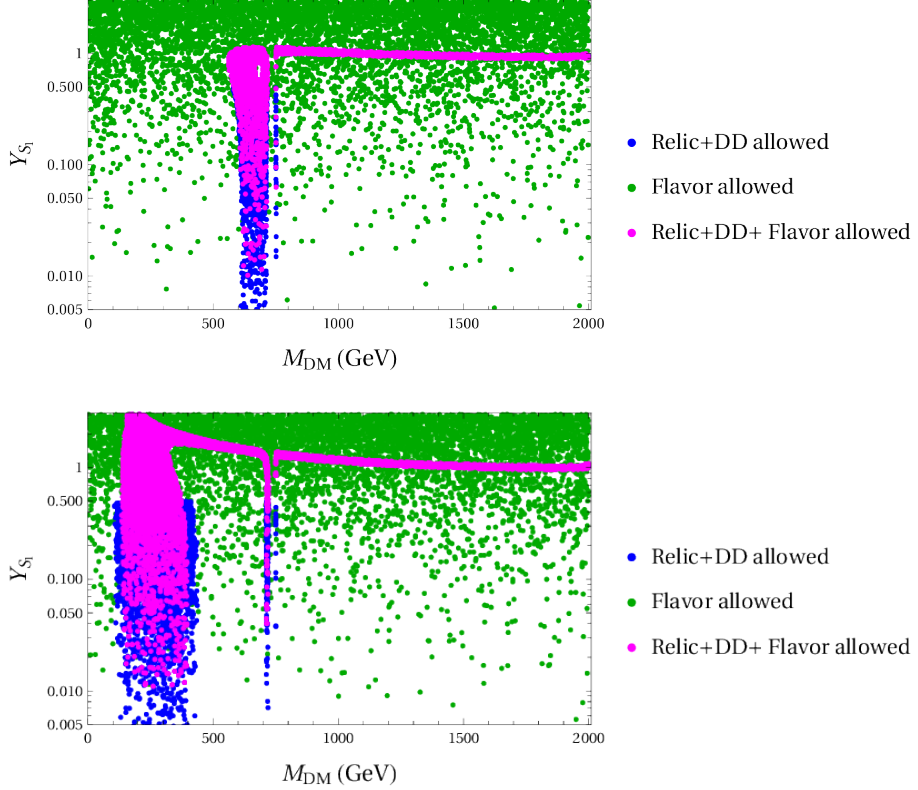


Figure 11: Allowed common parameter space in the plane of $M_{\text{DM}} - Y_{S_1}$ from both DM and flavor phenomenology for **Top Panel:** $\Delta M(\Psi_2, \Psi_1) = 1 \text{ GeV}$ and **Bottom Panel:** $\Delta M(\Psi_2, \Psi_1) = 10 \text{ GeV}$, with fixed parameters: $\lambda_S = 0.32$, $\lambda_{HS} = 1.29 \times 10^{-2}$, $\lambda_{S_1} = 10^{-2}$, $\lambda_{HS_1} = 10^{-4}$, $\lambda_{SS_1} = 10^{-10}$, $\sin \theta_{\text{DM}} = 0.001$, $m_s = 800 \text{ GeV}$, $m_{S_1} = 2 \text{ TeV}$, $M_{Z'} = 1.5 \text{ TeV}$, and $g_B = 0.05$.

We then examine the impact of the DM mass splitting on the structure of the allowed parameter space in the Y_{S_1} versus M_{DM} plane (Figure 11). For a small mass splitting $\Delta M(\Psi_2, \Psi_1) = 1 \text{ GeV}$ (**Top Panel**), the dark sector states remain nearly degenerate. As a consequence, the resonant features induced by DM annihilation and co-annihilation processes occur at closely spaced values of the DM mass. This leads to a pronounced clustering of resonance structures in the (Y_{S_1}, M_{DM}) plane, resulting in overlapping or narrowly separated allowed regions. In contrast, for a larger mass splitting $\Delta M(\Psi_2, \Psi_1) = 10 \text{ GeV}$ (**Bottom Panel**), the degeneracy between the dark sector states is lifted. This shifts the resonant conditions to distinct values of M_{DM} , thereby reducing the overlap between different resonance regions. Consequently, the allowed parameter space exhibits well-separated resonant bands. This behavior clearly illustrates the sensitivity of the model to the size of the mass splitting. In particular, a modest change in $\Delta M(\Psi_2, \Psi_1)$ from 1 GeV to 10 GeV qualitatively alters the structure of the allowed parameter space, highlighting the strong interplay between flavor and DM constraints. Based on these results, we randomly select a few benchmark points from the overall allowed regions of the parameter space and present them in tabular form in Tables 2 and 3 for Figs. 10 and 11, respectively.

6 Conclusion

In this work, we studied DM and flavor-physics phenomenology in a gauged theory of baryons with the inclusion of an additional colored scalar S_1 . We extended the Standard Model by a local $U(1)_B$ symmetry, a dark sector (consistent with anomaly cancellation), and a color-triplet scalar S_1 . The DM candidate is a mixed Dirac fermion arising from the mixing of singlet- and doublet-type exotic fermions, with the lightest state Ψ_1 being dominantly singlet-like. The baryonic gauge symmetry ensures the stability of the DM particle, while the extended particle content allows a simultaneous description of flavor and dark sector observables. The scalar S_1 here opens up novel interactions that can address the anomalies observed in $b \rightarrow s\mu^+\mu^-$ transitions. In particular, the exchange of S_1 generates the additional contributions to the Wilson coefficients C_9^{SM} and C_{10}^{SM} . In addition, S_1 plays an important role in DM phenomenology by opening additional coannihilation channels involving the dark-sector fermions. These processes are especially relevant when the mass splitting between dark-sector states is small, thereby significantly affecting the thermal freeze-out of DM and, in turn, its final relic abundance. Throughout our analysis, we assumed a negligible kinetic mixing between the SM Z boson and the $U(1)_B$ force carrier Z' .

A key feature of the model is the Yukawa interaction $Y_{S_1} \bar{q} S_1 \Psi_R$, which directly connects the dark sector to the quark sector. The same coupling Y_{S_1} controls both the size of the flavor-changing neutral current effects and the strength of the DM annihilation and coannihilation processes mediated by S_1 . As a result, the constraints from flavor observables and the relic density requirement jointly restrict the allowed parameter space, leading to correlated predictions for DM and flavor physics.

For the dark matter phenomenology, we performed extensive numerical scans to investigate the impact of the Yukawa coupling Y_{S_1} and the mass splittings between the fermionic states Ψ_1 and Ψ_2 , as well as between Ψ_1 and the scalar S_1 . We analyzed their effects on the resulting dark matter relic abundance and on constraints from direct and indirect detection experiments. From our analysis, we found that phenomenologically viable DM emerged for a mass range $m_{DM} \in [100 - 2000]$ GeV, with the $U(1)_B$ gauge coupling in the interval $g_B \in [0.02, 0.06]$ and the exotic Yukawa coupling in the range $Y_{S_1} \in [0.005, 1]$. These results were obtained by varying the fermionic mass splitting within $\Delta M(\Psi_2, \Psi_1) \in [1, 10]$ GeV, as summarized in Tables 2 and 3. Furthermore, we explored the dependence of the DM relic on the mass splittings as shown in Figures 3 and 4. We observed that for small values of mass splittings, $\Delta M(\Psi_2, \Psi_1) \& \Delta M(S_1, \Psi_1)$, i.e. when these $\Delta M \in [1-10]$ GeV, the obtained DM relic is within the 2σ PLANCK bound for a broad DM mass window in the range $M_{DM} \simeq 100-900$ GeV, while simultaneously satisfying latest constraints from direct and indirect detection experiments for the same parameter space as shown in Figs. 5, 6 and 7. Thus, the framework allows a significant parameter space and mass range for a cosmologically viable Dirac DM candidate that is allowed by the latest DD limits from LZ, particularly when coannihilation effects via next-to-lightest dark state and via S_1 are taken into account.

On the other hand, the analysis reveals a clear hierarchy between the constraints

arising from flavor observables and those from the dark sector. The flavor observables mediated by $b \rightarrow s\mu^+\mu^-$ transition decays allow a comparatively large region of parameter space. In contrast, the DM relic abundance and direct detection impose stronger bounds. Consequently, the common allowed parameter space consistent with both sectors is effectively governed by the dark contributions, with the flavor observables remaining close to their SM expectations throughout the region. Thus, the correlated structure of the model leads to several testable predictions. Additionally, the scalar S_1 can be probed at colliders through jet-plus-missing-energy signatures, while direct detection experiments test the Z' -mediated interactions of DM. Indirect searches, such as diffuse gamma-ray observations at the Cherenkov Telescope Array (CTA), provide complementary probes of the parameter space.

Finally, we note a few possible extensions of this work. The breaking of the $U(1)_B$ symmetry could proceed through a first-order phase transition, potentially giving rise to an observable stochastic gravitational-wave signal at upcoming experiments like LISA and ET. In addition, by carefully tuning the quantum numbers of exotic fermions, the framework can accommodate Majorana DM candidates too, which may lead to qualitatively different phenomenology and distinct indirect detection signatures, including loop-induced gamma-ray lines. Overall, the presented framework provides a simple, predictive setting in which DM and flavor physics phenomenology are closely linked, and its predictions within a given parameter space are falsifiable with upcoming CTA and XENONnT data.

Acknowledgment

Taramati acknowledges the financial support from the Department of Science and Technology, INSPIRE (DST/INSPIRE Fellowship/IF200289), New Delhi. MKM would like to acknowledge the financial support from the IoE PDRF at the University of Hyderabad. UP acknowledges SINP, Kolkata, as his current source of research funding. SP would like to acknowledge the funding support from SERB, Government of India, under the MATRICS project with grant no. MTR/2023/000687.

Appendix

A Relevant Feynman Diagrams due to extra scalar S_1

Here, we display the relevant Feynman diagrams contributing to DM annihilation and co-annihilation processes in the presence of the additional scalar S_1 . The diagrams include s - and t -channel processes mediated by scalar (h, s, S_1) and gauge (W^\pm, Z, Z') bosons, leading to quark, scalar, and gauge boson final states. These channels provide the dominant contributions to the DM relic abundance.

A.1 Feynman Diagrams Contributing to Relic Density

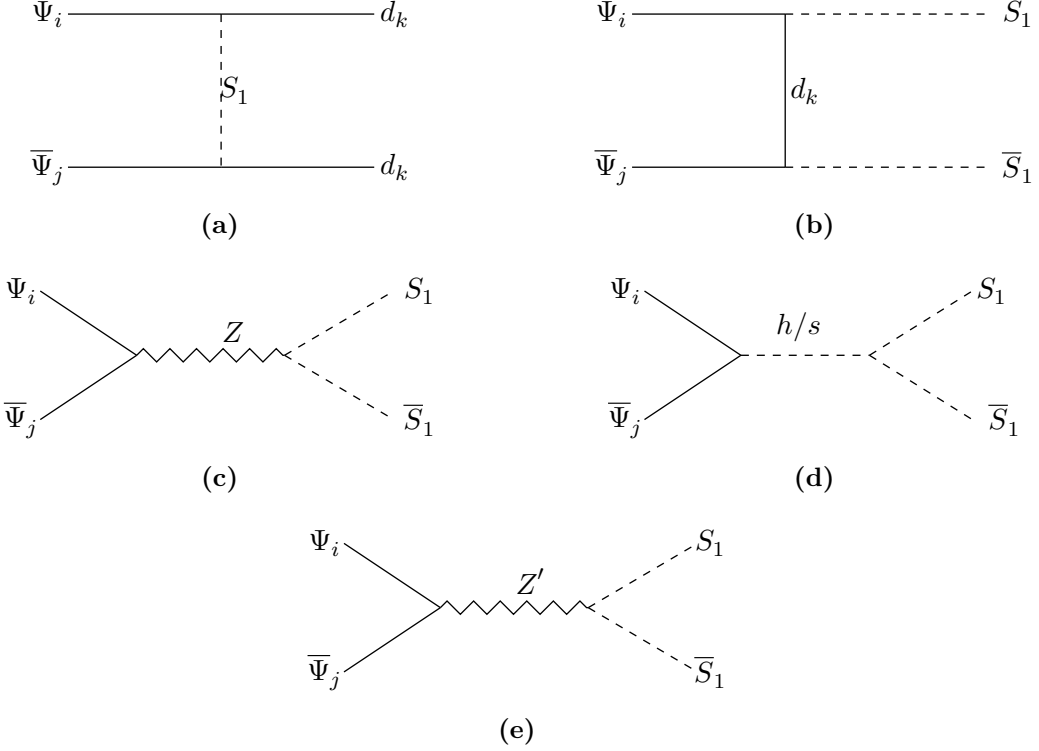


Figure 12: Feynman diagrams for annihilation ($i = j$) and co-annihilation ($i \neq j$) channels of dark fermion states into quarks and the exotic scalar S_1 , mediated by scalar (h, s) and gauge (Z, Z') bosons in the s - and t -channels.

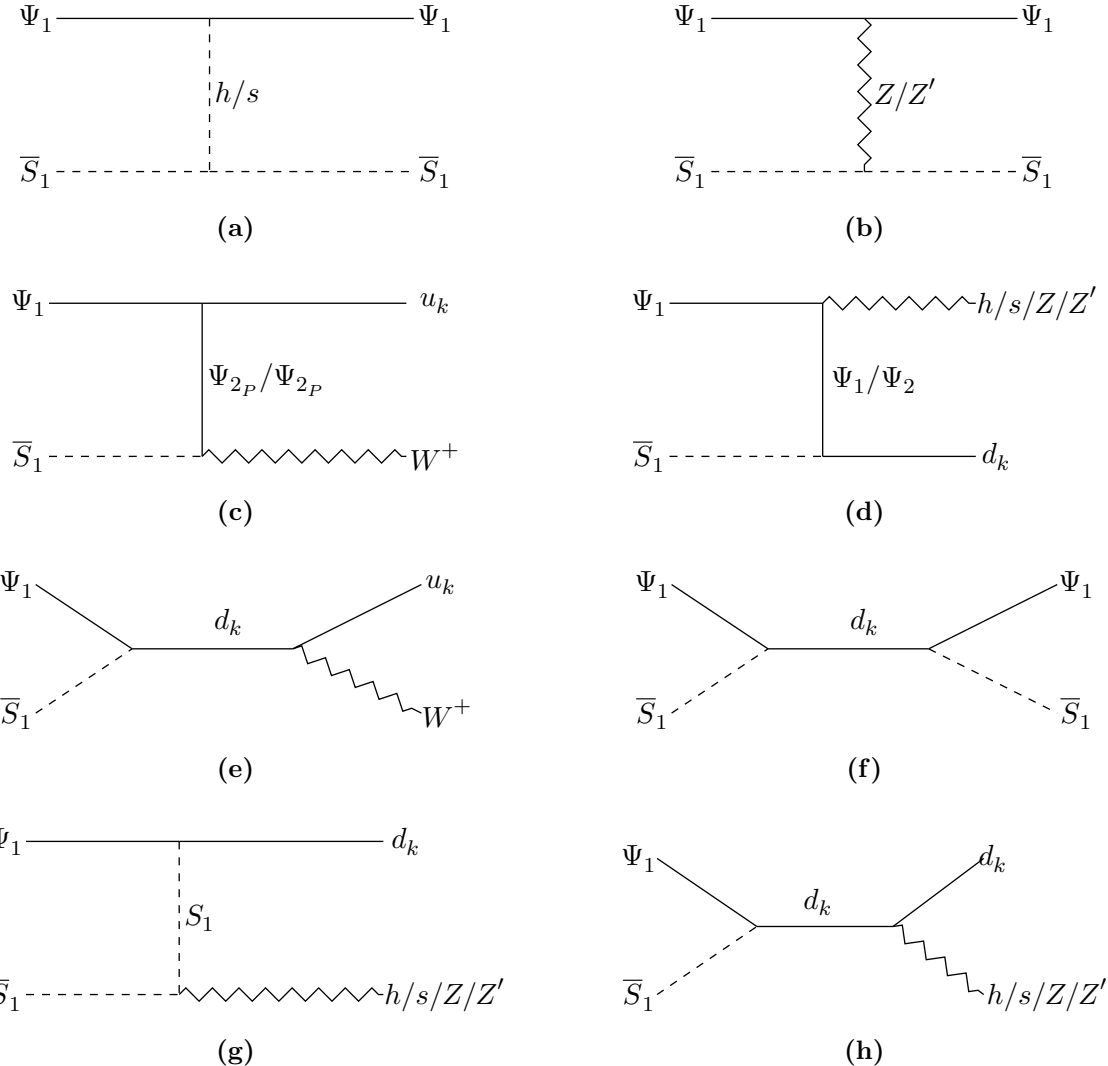


Figure 13: Dominant co-annihilation channels induced by the additional scalar S_1 involving the dark fermion Ψ_1 , mediated by scalar (h, s) and gauge (W^\pm, Z, Z') bosons, and leading to quark, scalar, and gauge boson final states. The index k labels the quark generation.

A.2 Relevant Feynman Diagrams with diffused gamma ray production

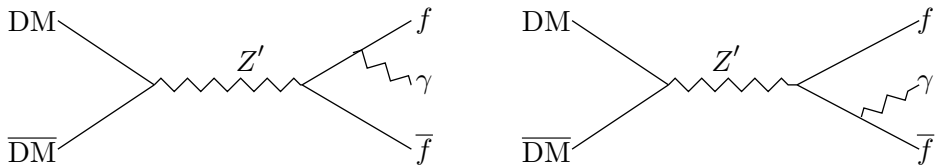


Figure 14: Feynman diagram illustrating DM annihilation into a fermion-antifermion pair accompanied by a photon, arising via final state radiation (FSR) at tree level. The fermion f can be either a Standard Model or an exotic fermion, and the process is mediated by the additional gauge boson Z' associated with the extended gauge symmetry.

B Details of the form factors and the angular coefficients for $B \rightarrow (P, V)\ell^+\ell^-$ processes

We provide the relevant form factors of $B \rightarrow K\ell^+\ell^-$ in B.1 and the angular coefficients of $B \rightarrow V\ell^+\ell^-$ processes in B.2 in term of the transverse amplitudes below.

B.1 Form factors for $B \rightarrow (K^{(*)}, \phi)\ell^+\ell^- (\ell = e, \mu, \tau)$

The hadronic matrix elements for the exclusive $B \rightarrow K$ transition in terms of form factors are given by [85]

$$\begin{aligned} J_\mu &= \langle K | \bar{s} \gamma^\mu b | B \rangle \\ &= f_+(q^2) \left[p_B^\mu + p_K^\mu - \frac{M_B^2 - M_K^2}{q^2} q^\mu \right] + f_0(q^2) \frac{M_B^2 - M_K^2}{q^2} q^\mu, \end{aligned} \quad (\text{B.1})$$

$$\begin{aligned} J_\mu^T &= \langle K | \bar{s} \sigma^{\mu\nu} q_\nu b | B \rangle \\ &= \frac{i f_T(q^2)}{M_B + M_K} \left[q^2 (p_B^\mu + p_K^\mu) - (M_B^2 - M_K^2) q^\mu \right]. \end{aligned} \quad (\text{B.2})$$

where $q = p_B - p_K$ with the mass of B and K mesons are M_B and M_K , respectively. The form factors given above the expression satisfy the following relations:

$$f_+(0) = f_0, \quad f_0(q^2) = f_+(q^2) + \frac{q^2}{M_B^2 - M_K^2} f_-(q^2). \quad (\text{B.3})$$

Similarly, for the $B \rightarrow V$ transition where ($V = K^*, \phi$), the hadronic matrix elements can be given in terms of the form factors as [97]

$$\begin{aligned} \langle V | \bar{s} \gamma^\mu b | B \rangle &= \frac{2 i V(q^2)}{M_B + M_V} \epsilon^{\mu\nu\rho\sigma} \epsilon_\nu^* p_{B_\rho} p_{V_\sigma}, \\ \langle V | \bar{s} \gamma^\mu \gamma_5 b | B \rangle &= 2 M_V A_0(q^2) \frac{\epsilon^* \cdot q}{q^2} q^\mu + (M_B + M_V) A_1(q^2) \left(\epsilon^{*\mu} - \frac{\epsilon^* \cdot q}{q^2} q^\mu \right) \\ &\quad - A_2(q^2) \frac{\epsilon^* \cdot q}{M_B + M_V} \left[p_B^\mu + p_V^\mu - \frac{M_B^2 - M_V^2}{q^2} q^\mu \right], \\ \langle V | \bar{s} i \sigma^{\mu\nu} q_\nu b | B \rangle &= 2 T_1(q^2) \epsilon^{\mu\nu\rho\sigma} \epsilon_\nu^* p_{B_\rho} p_{V_\sigma}, \\ \langle V | \bar{s} i \sigma^{\mu\nu} \gamma_5 q_\nu b | B \rangle &= T_2(q^2) \left[(M_B^2 - M_V^2) \epsilon^{*\mu} - (\epsilon^* \cdot q) (p_B^\mu + p_V^\mu) \right] \\ &\quad + T_3(q^2) (\epsilon^* \cdot q) \left[q^\mu - \frac{q^2}{M_B^2 - M_V^2} (p_B^\mu + p_V^\mu) \right], \end{aligned} \quad (\text{B.4})$$

where $q^\mu = (p_B^\mu - p_V^\mu)$ is the four momentum transfer and ϵ_μ is polarization vector of the V meson.

B.2 Angular coefficients

The q^2 dependent angular coefficients required for $B \rightarrow V \ell^+ \ell^- (\ell = \mu, e, \tau)$ processes are given as follows:

$$\begin{aligned}
I_1^c &= \left(|A_{L0}|^2 + |A_{R0}|^2 \right) + 8 \frac{m_l^2}{q^2} \text{Re} \left[A_{L0} A_{R0}^* \right] + 4 \frac{m_l^2}{q^2} |A_t|^2, \\
I_2^c &= -\beta_l^2 \left(|A_{L0}|^2 + |A_{R0}|^2 \right), \\
I_1^s &= \frac{3}{4} \left[|A_{L\perp}|^2 + |A_{L\parallel}|^2 + |A_{R\perp}|^2 + |A_{R\parallel}|^2 \right] \left(1 - \frac{4m_l^2}{3q^2} \right) + \frac{4m_l^2}{q^2} \text{Re} \left[A_{L\perp} A_{R\perp}^* + A_{L\parallel} A_{R\parallel}^* \right], \\
I_2^s &= \frac{1}{4} \beta_l^2 \left[|A_{L\perp}|^2 + |A_{L\parallel}|^2 + |A_{R\perp}|^2 + |A_{R\parallel}|^2 \right], \\
I_3^s &= \frac{1}{2} \beta_l^2 \left[|A_{L\perp}|^2 - |A_{L\parallel}|^2 + |A_{R\perp}|^2 - |A_{R\parallel}|^2 \right], \\
I_4 &= \frac{1}{\sqrt{2}} \beta_l^2 \left[\text{Re} \left(A_{L0} A_{L\parallel}^* \right) + \text{Re} \left(A_{R0} A_{R\parallel}^* \right) \right], \\
I_5 &= \sqrt{2} \beta_l \left[\text{Re} \left(A_{L0} A_{L\perp}^* \right) - \text{Re} \left(A_{R0} A_{R\perp}^* \right) \right], \\
I_6 &= 2 \beta_l \left[\text{Re} \left(A_{L\parallel} A_{L\perp}^* \right) - \text{Re} \left(A_{R\parallel} A_{R\perp}^* \right) \right], \\
I_7 &= \sqrt{2} \beta_l \left[\text{Im} \left(A_{L0} A_{L\parallel}^* \right) - \text{Im} \left(A_{R0} A_{R\parallel}^* \right) \right], \\
I_8 &= \frac{1}{\sqrt{2}} \beta_l^2 \left[\text{Im} \left(A_{L0} A_{L\perp}^* \right) + \text{Im} \left(A_{R0} A_{R\perp}^* \right) \right], \\
I_9 &= \beta_l^2 \left[\text{Im} \left(A_{L\parallel} A_{L\perp}^* \right) + \text{Im} \left(A_{R\parallel} A_{R\perp}^* \right) \right], \tag{B.5}
\end{aligned}$$

where $\beta_\ell = \sqrt{1 - 4m_\ell^2/q^2}$. According to Ref. [83], the transversity amplitude in terms of form factors and Wilson coefficients is given as

$$\begin{aligned}
A_{L0} &= N \frac{1}{2m_V \sqrt{q^2}} \left\{ (C_9^{eff} - C_{10}) \left[(M_B^2 - M_V^2 - q^2)(M_B + M_V)A_1 - \frac{\lambda}{M_B + M_V} A_2 \right] \right. \\
&\quad \left. + 2m_b C_7^{eff} \left[(M_B^2 + 3M_V^2 - q^2)T_2 - \frac{\lambda}{M_B^2 - M_V^2} T_3 \right] \right\}, \\
A_{L\perp} &= -N\sqrt{2} \left[(C_9^{eff} - C_{10}) \frac{\sqrt{\lambda}}{M_B + M_V} V + \frac{\sqrt{\lambda} 2m_b C_7^{eff}}{q^2} T_1 \right], \\
A_{L\parallel} &= N\sqrt{2} \left[(C_9^{eff} - C_{10})(M_B + M_V)A_1 + \frac{2m_b C_7^{eff}(M_B^2 - M_V^2)}{q^2} T_2 \right], \\
A_{Lt} &= N(C_9^{eff} - C_{10}) \frac{\sqrt{\lambda}}{\sqrt{q^2}} A_0, \tag{B.6}
\end{aligned}$$

$$\lambda = M_B^4 + M_V^4 + q^4 - 2 \left(M_B^2 M_V^2 + M_V^2 q^2 + q^2 M_B^2 \right)$$

and N , the normalization factor, which is defined as

$$N = \left[\frac{G_F^2 \alpha_{em}^2}{3 \cdot 2^{10} \pi^5 M_B^3} |V_{tb} V_{ts}^*|^2 q^2 \sqrt{\lambda} \left(1 - \frac{4m_l^2}{q^2} \right)^{1/2} \right]^{1/2}. \quad (\text{B.7})$$

The right chiral component A_{Ri} of the transversity amplitudes can be obtained by replacing A_{Li} by $A_{Li}|_{C_{10} \rightarrow -C_{10}} (i = 0, \parallel, \perp, t)$.

References

- [1] M. Cirelli, A. Strumia and J. Zupan, *Dark Matter*, [2406.01705](#).
- [2] D. Abercrombie et al., *Dark Matter benchmark models for early LHC Run-2 Searches: Report of the ATLAS/CMS Dark Matter Forum*, *Phys. Dark Univ.* **27** (2020) 100371 [[1507.00966](#)].
- [3] P. Fileviez Pérez, E. Golias, R.-H. Li, C. Murgui and A.D. Plascencia, *Anomaly-free dark matter models*, *Phys. Rev. D* **100** (2019) 015017 [[1904.01017](#)].
- [4] C. Murgui Galvez, *Phenomenological and cosmological aspects of electroweak models beyond the Standard Model*, Ph.D. thesis, Valencia U., 2020.
- [5] Taramati, R. Sahu, U. Patel, K. Ghosh and S. Patra, *Singlet-doublet fermionic dark matter in gauge theory of baryons*, [2408.12424](#).
- [6] Taramati, L. Malhotra, Z.A. Borboruah and S. Patra, *Probing Leptophobic Dark Sectors via Gravitational Wave Signatures*, [2508.17476](#).
- [7] G. Bertone, D. Hooper and J. Silk, *Particle dark matter: Evidence, candidates and constraints*, *Phys. Rept.* **405** (2005) 279 [[hep-ph/0404175](#)].
- [8] G. Bertone and D. Hooper, *History of dark matter*, *Rev. Mod. Phys.* **90** (2018) 045002 [[1605.04909](#)].
- [9] A. Das, S. Gola, S. Mandal and N. Sinha, *Two-component scalar and fermionic dark matter candidates in a generic $U(1)X$ model*, *Phys. Lett. B* **829** (2022) 137117 [[2202.01443](#)].
- [10] S. Patra, W. Rodejohann and C.E. Yaguna, *A new $B - L$ model without right-handed neutrinos*, *JHEP* **09** (2016) 076 [[1607.04029](#)].
- [11] U. Patel, Avnish, S. Patra and K. Ghosh, *Multipartite dark matter in a gauge theory of leptons*, *JHEP* **04** (2025) 079 [[2407.06737](#)].
- [12] A. Das, S. Goswami, K.N. Vishnudath and T. Nomura, *Constraining a general $U(1)'$ inverse seesaw model from vacuum stability, dark matter and collider*, *Phys. Rev. D* **101** (2020) 055026 [[1905.00201](#)].
- [13] A. Alves, A. Berlin, S. Profumo and F.S. Queiroz, *Dirac-fermionic dark matter in $U(1)_X$ models*, *JHEP* **10** (2015) 076 [[1506.06767](#)].
- [14] N. Okada, S. Okada and Q. Shafi, *Light z' and dark matter from $u(1)_X$ gauge symmetry*, *Physics Letters B* **810** (2020) 135845.
- [15] M.J. Neves, N. Okada and S. Okada, *Majorana fermion dark matter in minimally extended left-right symmetric model*, *JHEP* **09** (2021) 038 [[2103.08873](#)].

- [16] J. Lao, C. Cai, Z.-H. Yu, Y.-P. Zeng and H.-H. Zhang, *Fermionic and scalar dark matter with hidden $u(1)$ gauge interaction and kinetic mixing*, *Phys. Rev. D* **101** (2020) 095031.
- [17] A. Biswas, S. Ganguly and S. Roy, *Fermionic dark matter via uv and ir freeze-in and its possible x-ray signature*, *Journal of Cosmology and Astroparticle Physics* **2020** (2020) 043.
- [18] A. Das, S.K. Gola, S. Mandal and N. Sinha, *Two-component scalar and fermionic dark matter candidates in a generic $u(1)$ model*, *Physics Letters B* (2022) .
- [19] B.L. Sánchez-Vega and E.R. Schmitz, *Fermionic dark matter and neutrino masses in a $\mathcal{B} - \mathcal{L}$ model*, *Phys. Rev. D* **92** (2015) 053007.
- [20] S. Mishra, M.K. Behera, R. Mohanta, S. Patra and S. Singirala, *Neutrino phenomenology and dark matter in an A_4 flavour extended $B - L$ model*, *Eur. Phys. J. C* **80** (2020) 420 [[1907.06429](#)].
- [21] E. Ma, P.K. Paul and N. Sahu, *Naturally small Dirac neutrino mass and $B - L$ dark matter*, [2601.05926](#).
- [22] S. Mahapatra, P.K. Paul, N. Sahu and P. Shukla, *Verifiable type-III seesaw and dark matter in a gauged $U(1)_{B-L}$ symmetric model*, [2504.00109](#).
- [23] CCM COLLABORATION collaboration, *First leptophobic dark matter search from the coherent-captain-mills liquid argon detector*, *Phys. Rev. Lett.* **129** (2022) 021801.
- [24] P. Fileviez Perez and M.B. Wise, *Breaking Local Baryon and Lepton Number at the TeV Scale*, *JHEP* **08** (2011) 068 [[1106.0343](#)].
- [25] E. Ma, *Gauged baryon number and dibaryonic dark matter*, *Phys. Lett. B* **813** (2021) 136066 [[2011.13887](#)].
- [26] L. Michaels and F. Yu, *Probing new $U(1)$ gauge symmetries via exotic $Z \rightarrow Z' \gamma$ decays*, *JHEP* **03** (2021) 120 [[2010.00021](#)].
- [27] J. Boos, C.D. Carone, N.L. Donald and M.R. Musser, *Asymptotically safe dark matter with gauged baryon number*, *Phys. Rev. D* **107** (2023) 035018 [[2209.14268](#)].
- [28] P. Fileviez Pérez, E. Golias, R.-H. Li and C. Murgui, *Leptophobic Dark Matter and the Baryon Number Violation Scale*, *Phys. Rev. D* **99** (2019) 035009 [[1810.06646](#)].
- [29] J. Butterworth, H. Debnath, P. Fileviez Perez and Y. Yeh, *Dark matter from anomaly cancellation at the LHC*, *Phys. Rev. D* **110** (2024) 075001 [[2405.03749](#)].
- [30] J. Butterworth, H. Debnath, J. Egan and P. Fileviez Perez, *Local baryon number at the LHC*, *Phys. Rev. D* **112** (2025) 015012 [[2505.06341](#)].
- [31] DARWIN collaboration, *DARWIN: direct dark matter search with the ultimate detector*, *J. Phys. Conf. Ser.* **1468** (2020) 012068.
- [32] DARKSIDE-20K collaboration, *DarkSide-20k: A 20 tonne two-phase LAr TPC for direct dark matter detection at LNGS*, *Eur. Phys. J. Plus* **133** (2018) 131 [[1707.08145](#)].
- [33] BELLE-II collaboration, *The Belle II Experiment at SuperKEKB – Input to the European Particle Physics Strategy*, [2503.24155](#).
- [34] LHCb collaboration, *The LHCb Upgrade I*, *JINST* **19** (2024) P05065 [[2305.10515](#)].
- [35] M. Bordone, G. Isidori and A. Pattori, *On the Standard Model predictions for R_K and R_{K^*}* , *Eur. Phys. J. C* **76** (2016) 440 [[1605.07633](#)].

[36] G. Hiller and F. Kruger, *More model-independent analysis of $b \rightarrow s$ processes*, *Phys. Rev. D* **69** (2004) 074020 [[hep-ph/0310219](#)].

[37] LHCb collaboration, *Measurement of lepton universality parameters in $B^+ \rightarrow K^+ \ell^+ \ell^-$ and $B^0 \rightarrow K^{*0} \ell^+ \ell^-$ decays*, *Phys. Rev. D* **108** (2023) 032002 [[2212.09153](#)].

[38] LHCb collaboration, *Tests of lepton universality using $B^0 \rightarrow K_S^0 \ell^+ \ell^-$ and $B^+ \rightarrow K^{*+} \ell^+ \ell^-$ decays*, *Phys. Rev. Lett.* **128** (2022) 191802 [[2110.09501](#)].

[39] D.M. Straub, *flavio: a Python package for flavour and precision phenomenology in the Standard Model and beyond*, [1810.08132](#).

[40] LHCb collaboration, *Test of Lepton Flavor Universality with $Bs0 \rightarrow \phi \ell^+ \ell^-$ Decays*, *Phys. Rev. Lett.* **134** (2025) 121803 [[2410.13748](#)].

[41] S. Descotes-Genon, T. Hurth, J. Matias and J. Virto, *Optimizing the basis of $B \rightarrow K^* ll$ observables in the full kinematic range*, *JHEP* **05** (2013) 137 [[1303.5794](#)].

[42] LHCb collaboration, *Measurement of CP-Averaged Observables in the $B^0 \rightarrow K^{*0} \mu^+ \mu^-$ Decay*, *Phys. Rev. Lett.* **125** (2020) 011802 [[2003.04831](#)].

[43] S. Descotes-Genon, J. Matias, M. Ramon and J. Virto, *Implications from clean observables for the binned analysis of $B^- \rightarrow K^* \mu^+ \mu^-$ at large recoil*, *JHEP* **01** (2013) 048 [[1207.2753](#)].

[44] CMS collaboration, *Measurement of angular parameters from the decay $B^0 \rightarrow K^{*0} \mu^+ \mu^-$ in proton-proton collisions at $\sqrt{s} = 8$ TeV*, *Phys. Lett. B* **781** (2018) 517 [[1710.02846](#)].

[45] S. Descotes-Genon, L. Hofer, J. Matias and J. Virto, *On the impact of power corrections in the prediction of $B \rightarrow K^* \mu^+ \mu^-$ observables*, *JHEP* **12** (2014) 125 [[1407.8526](#)].

[46] BELLE collaboration, *Angular analysis of $B^0 \rightarrow K^*(892)^0 \ell^+ \ell^-$, in LHC Ski 2016: A First Discussion of 13 TeV Results*, 4, 2016 [[1604.04042](#)].

[47] HPQCD collaboration, *Standard Model predictions for $B \rightarrow K \ell^+ \ell^-$, $B \rightarrow K \ell 1 \ell 2 +$ and $B \rightarrow K \nu \nu^-$ using form factors from $N_f=2+1+1$ lattice QCD*, *Phys. Rev. D* **107** (2023) 014511 [[2207.13371](#)].

[48] A. Bharucha, D.M. Straub and R. Zwicky, *$B \rightarrow V \ell^+ \ell^-$ in the Standard Model from light-cone sum rules*, *JHEP* **08** (2016) 098 [[1503.05534](#)].

[49] LHCb collaboration, *Measurements of the S-wave fraction in $B^0 \rightarrow K^+ \pi^- \mu^+ \mu^-$ decays and the $B^0 \rightarrow K^*(892)^0 \mu^+ \mu^-$ differential branching fraction*, *JHEP* **11** (2016) 047 [[1606.04731](#)].

[50] J. Aebischer, J. Kumar, P. Stangl and D.M. Straub, *A Global Likelihood for Precision Constraints and Flavour Anomalies*, *Eur. Phys. J. C* **79** (2019) 509 [[1810.07698](#)].

[51] LHCb collaboration, *Branching Fraction Measurements of the Rare $B_s^0 \rightarrow \phi \mu^+ \mu^-$ and $B_s^0 \rightarrow f_2'(1525) \mu^+ \mu^-$ Decays*, *Phys. Rev. Lett.* **127** (2021) 151801 [[2105.14007](#)].

[52] LHCb collaboration, *Differential branching fraction and angular analysis of the decay $B_s^0 \rightarrow \phi \mu^+ \mu^-$* , *JHEP* **07** (2013) 084 [[1305.2168](#)].

[53] LHCb collaboration, *Angular analysis and differential branching fraction of the decay $B_s^0 \rightarrow \phi \mu^+ \mu^-$* , *JHEP* **09** (2015) 179 [[1506.08777](#)].

[54] C. Bobeth, M. Gorbahn, T. Hermann, M. Misiak, E. Stamou and M. Steinhauser, *$B_{s,d} \rightarrow l^+ l^-$ in the Standard Model with Reduced Theoretical Uncertainty*, *Phys. Rev. Lett.* **112** (2014) 101801 [[1311.0903](#)].

[55] M. Beneke, C. Bobeth and R. Szafron, *Power-enhanced leading-logarithmic QED corrections to $B_q \rightarrow \mu^+ \mu^-$* , *JHEP* **10** (2019) 232 [[1908.07011](#)].

[56] A. Greljo, J. Salko, A. Smolkovič and P. Stangl, *Rare b decays meet high-mass Drell-Yan*, *JHEP* **05** (2023) 087 [[2212.10497](#)].

[57] S. Singirala, S. Sahoo and R. Mohanta, *Exploring dark matter, neutrino mass and $R_{K^{(*)},\phi}$ anomalies in $L_\mu - L_\tau$ model*, *Phys. Rev. D* **99** (2019) 035042 [[1809.03213](#)].

[58] S. Singirala, S. Sahoo and R. Mohanta, *Light dark matter, rare B decays with missing energy in $L\mu$ - $L\tau$ model with a scalar leptoquark*, *Phys. Rev. D* **105** (2022) 015033 [[2106.03735](#)].

[59] M.K. Mohapatra, S. Singirala, D. Panda and R. Mohanta, *Correlative study of flavor anomalies and dark matter in the light of scalar leptoquark*, [2409.16961](#).

[60] W. Chao, H. Wang, L. Wang and Y. Zhang, *Dark matter, Z' , vector-like quark at the LHC and $b \rightarrow s\mu\mu$ anomaly*, *Chin. Phys. C* **45** (2021) 083105 [[2102.07518](#)].

[61] P. Ko, T. Nomura and H. Okada, *Muon $g - 2$, $B \rightarrow K^{(*)}\mu^+ \mu^-$ anomalies, and leptophilic dark matter in $U(1)_{\mu-\tau}$ gauge symmetry*, *JHEP* **05** (2022) 098 [[2110.10513](#)].

[62] S. Sahoo, S. Singirala and R. Mohanta, *Dark matter and flavor anomalies in the light of vector-like fermions and scalar leptoquark*, [2112.04382](#).

[63] A. Hook, E. Izaguirre and J.G. Wacker, *Model Independent Bounds on Kinetic Mixing*, *Adv. High Energy Phys.* **2011** (2011) 859762 [[1006.0973](#)].

[64] T. Gherghetta, J. Kersten, K. Olive and M. Pospelov, *Evaluating the price of tiny kinetic mixing*, *Phys. Rev. D* **100** (2019) 095001.

[65] M. Napsuciale, S. Rodríguez and H. Hernández-Arellano, *Kinetic mixing, custodial symmetry, and a lower bound on the mass of a dark gauge boson*, *Progress of Theoretical and Experimental Physics* **2022** (2022) 093E01 [<https://academic.oup.com/ptep/article-pdf/2022/9/093E01/45911873/ptac117.pdf>].

[66] F. Staub, *SARAH 4 : A tool for (not only SUSY) model builders*, *Comput. Phys. Commun.* **185** (2014) 1773 [[1309.7223](#)].

[67] W. Porod and F. Staub, *SPheno 3.1: Extensions including flavour, CP-phases and models beyond the MSSM*, *Comput. Phys. Commun.* **183** (2012) 2458 [[1104.1573](#)].

[68] G. Bélanger, F. Boudjema, A. Goudelis, A. Pukhov and B. Zaldivar, *micrOMEGAs5.0 : Freeze-in*, *Comput. Phys. Commun.* **231** (2018) 173 [[1801.03509](#)].

[69] PLANCK collaboration, *Planck 2018 results. VI. Cosmological parameters*, *Astron. Astrophys.* **641** (2020) A6 [[1807.06209](#)].

[70] LZ collaboration, *First Dark Matter Search Results from the LUX-ZEPLIN (LZ) Experiment*, *Phys. Rev. Lett.* **131** (2023) 041002 [[2207.03764](#)].

[71] XENON collaboration, *Dark Matter Search Results from a One Ton-Year Exposure of XENON1T*, *Phys. Rev. Lett.* **121** (2018) 111302 [[1805.12562](#)].

[72] XENON collaboration, *Projected WIMP sensitivity of the XENONnT dark matter experiment*, *JCAP* **11** (2020) 031 [[2007.08796](#)].

[73] A.W. Strong, R. Diehl, H. Halloin, V. Schoenfelder, L. Bouchet, P. Mandrou et al., *Gamma-ray continuum emission from the inner galactic region as observed with integral/spi*, *Astron. Astrophys.* **444** (2005) 495 [[astro-ph/0509290](#)].

[74] VERITAS collaboration, *Observation of Galactic Gamma-ray Sources with VERITAS*, *AIPI Conf. Proc.* **1085** (2009) 187 [[0810.0515](#)].

[75] D.J. Thompson, *Gamma ray astrophysics: the EGRET results*, *Rept. Prog. Phys.* **71** (2008) 116901 [[0811.0738](#)].

[76] FERMI-LAT collaboration, *Constraining Dark Matter Models from a Combined Analysis of Milky Way Satellites with the Fermi Large Area Telescope*, *Phys. Rev. Lett.* **107** (2011) 241302 [[1108.3546](#)].

[77] FERMI-LAT collaboration, *Fermi Large Area Telescope Third Source Catalog*, *Astrophys. J. Suppl.* **218** (2015) 23 [[1501.02003](#)].

[78] H.E.S.S. collaboration, *Discovery of very-high-energy gamma-rays from the galactic centre ridge*, *Nature* **439** (2006) 695 [[astro-ph/0603021](#)].

[79] H.E.S.S. collaboration, *Search for Photon-Linelike Signatures from Dark Matter Annihilations with H.E.S.S.*, *Phys. Rev. Lett.* **110** (2013) 041301 [[1301.1173](#)].

[80] CTA CONSORTIUM collaboration, B.S. Acharya et al., *Science with the Cherenkov Telescope Array*, WSP (11, 2018), 10.1142/10986, [[1709.07997](#)].

[81] CTAO collaboration, *Dark matter line searches with the Cherenkov Telescope Array*, *JCAP* **07** (2024) 047 [[2403.04857](#)].

[82] A. Ali, P. Ball, L.T. Handoko and G. Hiller, *A Comparative study of the decays $B \rightarrow (K, K^*)\ell^+\ell^-$ in standard model and supersymmetric theories*, *Phys. Rev. D* **61** (2000) 074024 [[hep-ph/9910221](#)].

[83] W. Altmannshofer, P. Ball, A. Bharucha, A.J. Buras, D.M. Straub and M. Wick, *Symmetries and Asymmetries of $B \rightarrow K^*\mu^+\mu^-$ Decays in the Standard Model and Beyond*, *JHEP* **01** (2009) 019 [[0811.1214](#)].

[84] S. Sahoo and R. Mohanta, *Study of the rare semileptonic decays $B_d^0 \rightarrow K^*\ell^+\ell^-$ in scalar leptoquark model*, *Phys. Rev. D* **93** (2016) 034018 [[1507.02070](#)].

[85] HPQCD collaboration, *Rare decay $B \rightarrow K\ell^+\ell^-$ form factors from lattice QCD*, *Phys. Rev. D* **88** (2013) 054509 [[1306.2384](#)].

[86] S. Descotes-Genon, L. Hofer, J. Matias and J. Virto, *Global analysis of $b \rightarrow s\ell\ell$ anomalies*, *JHEP* **06** (2016) 092 [[1510.04239](#)].

[87] B. Capdevila, S. Descotes-Genon, J. Matias and J. Virto, *Assessing lepton-flavour non-universality from $B \rightarrow K^*\ell\ell$ angular analyses*, *JHEP* **10** (2016) 075 [[1605.03156](#)].

[88] LHCb collaboration, *Measurement of the $B_s^0 \rightarrow \mu^+\mu^-$ decay properties and search for the $B^0 \rightarrow \mu^+\mu^-$ and $B_s^0 \rightarrow \mu^+\mu^-\gamma$ decays*, *Phys. Rev. D* **105** (2022) 012010 [[2108.09283](#)].

[89] ATLAS collaboration, *Study of the rare decays of B_s^0 and B^0 mesons into muon pairs using data collected during 2015 and 2016 with the ATLAS detector*, *JHEP* **04** (2019) 098 [[1812.03017](#)].

[90] CMS collaboration, *Measurement of properties of $B_s^0 \rightarrow \mu^+\mu^-$ decays and search for $B^0 \rightarrow \mu^+\mu^-$ with the CMS experiment*, *JHEP* **04** (2020) 188 [[1910.12127](#)].

[91] LHCb collaboration, *Measurement of the $B_s^0 \rightarrow \mu^+\mu^-$ branching fraction and effective lifetime and search for $B^0 \rightarrow \mu^+\mu^-$ decays*, *Phys. Rev. Lett.* **118** (2017) 191801 [[1703.05747](#)].

[92] LHCb collaboration, *Differential branching fractions and isospin asymmetries of $B \rightarrow K^{(*)}\mu^+\mu^-$ decays*, *JHEP* **06** (2014) 133 [[1403.8044](#)].

- [93] LHCb collaboration, *Angular analysis of the $B^0 \rightarrow K^{*0} \mu^+ \mu^-$ decay using 3 fb^{-1} of integrated luminosity*, *JHEP* **02** (2016) 104 [[1512.04442](#)].
- [94] LHCb collaboration, *Angular Analysis of the $B^+ \rightarrow K^{*+} \mu^+ \mu^-$ Decay*, *Phys. Rev. Lett.* **126** (2021) 161802 [[2012.13241](#)].
- [95] LHCb collaboration, *Angular analysis of the rare decay $B_s^0 \rightarrow \phi \mu^+ \mu^-$* , *JHEP* **11** (2021) 043 [[2107.13428](#)].
- [96] BELLE collaboration, *Lepton-Flavor-Dependent Angular Analysis of $B \rightarrow K^* \ell^+ \ell^-$* , *Phys. Rev. Lett.* **118** (2017) 111801 [[1612.05014](#)].
- [97] D. Ebert, R.N. Faustov and V.O. Galkin, *Rare Semileptonic Decays of B and B_c Mesons in the Relativistic Quark Model*, *Phys. Rev. D* **82** (2010) 034032 [[1006.4231](#)].